Solvent-Templated Methylammonium-Based Ruddlesden-Popper Perovskites with Short Interlayer Distances

Ayan A. Zhumekenov,[1] Yongxin Li,[2] Yifan Zhou,[5] Natalia Yantara,[3] Anil Kanwat,[3] Benny Febriansyah,[3] Darrell Jun Jie Tay,[1,4] Hesham R. Abuzeid,[1] Yeow Boon Tay,[1] Emha Bayu Miftahullatif,[1] Kedar Hippalgaonkar,[1] Sumod A. Pullarkat,[2] Jun Yin,[5,] Nripan Mathews[1,3,*]*

[1] School of Materials Science and Engineering (MSE), Nanyang Technological University, 50 Nanyang Avenue, Singapore 639798
[2] School of Physical and Mathematical Sciences (SPMS), Nanyang Technological University, Singapore 637371
[3] Energy Research Institute at Nanyang Technological University (ERI@N), Research Techno Plaza, X-Frontier Block Level 5, 50 Nanyang Drive, Singapore 637553
[4] Interdisciplinary Graduate School (IGS), Nanyang Technological University, 50 Nanyang Avenue, Singapore 639798
[5] Department of Applied Physics, The Hong Kong Polytechnic University, Hung Hom, Kowloon, Hong Kong 999077, China

* Corresponding authors: nripan@ntu.edu.sg, jun.yin@polyu.edu.hk

ABSTRACT. Two-dimensional (2D) halide perovskites are exquisite semiconductors with great structural tunability. They can incorporate a rich variety of organic species that not only template their layered structures but also add new functionalities to their optoelectronic characteristics. Here, we present a series of new methylammonium ($CH_3NH_3^+$ or MA)-based 2D Ruddlesden-Popper perovskites templated by dimethyl carbonate ($CH_3OCOOCH_3$ or DMC) solvent molecules. We report the synthesis, detailed structural analysis, and characterization of four new compounds: $MA_2(DMC)PbI_4$ (n=1), $MA_3(DMC)Pb_2I_7$ (n=2), $MA_4(DMC)Pb_3I_{10}$ (n=3), and $MA_3(DMC)Pb_2Br_7$ (n=2). Notably, these compounds represent unique structures with MA as the sole organic cation both within and between the perovskite sheets, while DMC molecules occupy a tight space between the MA cations in the interlayer. They form hydrogen-bonded $[MA\cdots DMC\cdots MA]^{2+}$ complexes that act as spacers preventing the perovskite sheets from condensing into each other. We report one of the shortest interlayer distances (~5.7–5.9 Å) in solvent-incorporated 2D halide perovskites. Furthermore, the synthesized crystals exhibit similar optical characteristics to other 2D perovskite systems, including narrow photoluminescence (PL) signals. The density functional theory (DFT) calculations confirm their direct-bandgap nature. Meanwhile, the phase stability of these systems was found to correlate with the H-bond distances and their strengths, decreasing in the order: $MA_3(DMC)Pb_2I_7$ > $MA_4(DMC)Pb_3I_{10}$ > $MA_2(DMC)PbI_4$ ~ $MA_3(DMC)Pb_2Br_7$. The relatively loosely bound nature of DMC molecules enables us to design a thermochromic cell that can withstand 25 cycles of switching between two colored states. This work exemplifies the unconventional role of the non-charged solvent molecule in templating the 2D perovskite structure.

TOC GRAPHICS

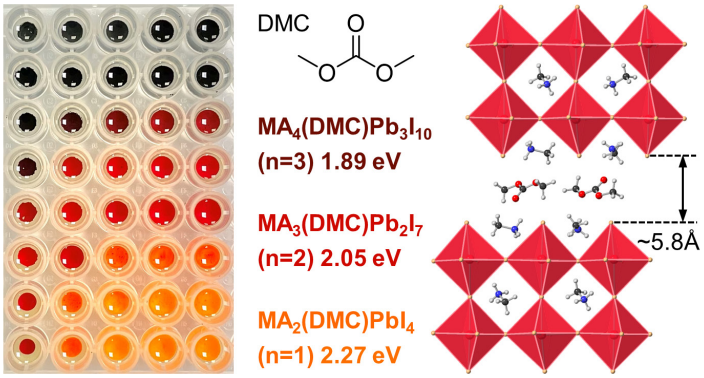

INTRODUCTION

Halide perovskites have recently emerged as the next-generation solution-processable semiconductors with excellent characteristics suitable for a range of technological applications including solar cells, light-emitting devices, high-energy (X-ray and γ-ray) detectors, and memristors.[1–4] The most extensively studied three-dimensional (3D) halide perovskites with the general chemical formula of ABX_3 (where A = $CH_3NH_3^+$ or MA, $CH(NH_2)_2^+$ or FA, Cs^+; B = Pb^{2+}, Sn^{2+}, Ge^{2+}; X = Cl^-, Br^-, I^-) feature a 3D structure composed of corner-shared $[BX_{6/2}]$-octahedra and A-site cations occupying the cages between the octahedra.[5,6] Meanwhile, two-dimensional (2D) halide perovskites with the general chemical formula of $(L)_{2/q}(A)_{n-1}B_nX_{3n+1}$ derive from their 3D counterparts by 'slicing' the perovskite lattice along specific crystallographic directions, typically <100>, <110>, and <111>, and then stacking the obtained $[B_nX_{3n+1}]$ perovskite sheets, or slabs, of thickness *n* with bulky organic cations (L), or 'spacers', with the charge of *q*=+1 or +2, to form a layered structure.[7–9]

Due to geometrical factors, there are only few choices for A-site cations in lead-based 3D perovskites. Among them, methylammonium ($CH_3NH_3^+$ or MA) has long been known as a 'perovskitizer' for its ability to template the 3D perovskite lattice.[7,10] By contrast, cesium (Cs^+) and formamidinium ($CH(NH_2)_2^+$ or FA) can form both 3D and 2D structures.[11–13] Meanwhile, slightly larger cations such as ethylammonium ($CH_3CH_2NH_3^+$ or EA) and dimethylammonium ($(CH_3)_2NH_2^+$ or DMA) cannot form a standalone 3D phase but can still be incorporated into the structure of 2D perovskites as A-site cations.[14–16] In general, 2D perovskites are chemically and structurally more diverse than their 3D counterparts. A plethora of 2D perovskite structures, including Ruddlesden-Popper (RP) (when *q*=1), Dion-Jacobson (DJ) (when *q*=2), and alternating cation in the interlayer (ACI) phases, with various spacers and diverse properties have been reported over the years.[7–9] The generally hydrophobic nature of those spacers also provides relatively better stability to 2D perovskites with respect to their 3D counterparts.

In early examples of 2D halide perovskites, simple spacers such as butylammonium ($C_4H_9NH_3^+$ or BA) and phenethylammonium ($C_6H_5CH_2CH_2NH_3^+$ or PEA) cations were used.[17–20] These spacers typically act as insulating barriers between the semiconducting perovskite sheets, making 2D perovskites intrinsic multiple quantum wells (MQWs). Meanwhile, more recent developments include spacers with added functionalities beyond their ability to template the 2D perovskite

structure. For instance, the incorporation of organic cations with electron-rich chromophore moieties, such as oligothiophenes and pyrenes,[21–24] have shown to greatly improve the out-of-plane charge transfer in 2D halide perovskites, which is highly essential for their applications in solar cells. However, these functionalities are not solely limited to the choice of a spacer cation. In fact, organic interlayers between the perovskite sheets, as a whole, have a huge room for both synthetic and post-synthetic modifications that could potentially reveal new properties and phenomena in 2D halide perovskites.[25]

An interesting approach towards introducing new functionalities in 2D halide perovskites is to structurally incorporate external guest molecules or other non-charged species in their organic interlayers. For instance, in 1980s, Dolzhenko *et al.* were first to post-synthetically intercalate solvent molecules between the sheets of a 2D perovskite.[17] Later, Mitzi *et al.* showed analogous effect with slightly improved intercalation and de-intercalation processes.[26] Since then, different molecular species, including dimethyl sulfoxide (DMSO), have been incorporated into the structure of 2D perovskites during or post their synthesis.[27–30] Meanwhile, in 2014, Karunadasa *et al.* reported an approach where they were able to covalently bind the intercalated halogen molecules to the interlayer cations.[31,32] Very recently, their team have also demonstrated the templated growth of low-dimensional non-perovskite phases between the sheets of 2D perovskites, thus, constructing the first perovskite–non-perovskite 2D heterostructures.[33] The intergrowth of two phases is ensured by their matching lattice parameters.

Inspired by these design concepts, we present a series of new solvent-templated 2D Ruddlesden-Popper perovskites with the general chemical formula of $MA_{n+1}(DMC)Pb_nX_{3n+1}$ (where MA is methylammonium ($CH_3NH_3^+$); DMC is dimethyl carbonate ($CH_3OCOOCH_3$); X = Br^-, I^-; and *n*=1,2,3). We successfully grow phase-pure $MA_2(DMC)PbI_4$ (n=1 iodide), $MA_3(DMC)Pb_2I_7$ (n=2 iodide), $MA_4(DMC)Pb_3I_{10}$ (n=3 iodide), and $MA_3(DMC)Pb_2Br_7$ (n=2 bromide) crystals by two different crystallization strategies and determine the conditions for one of them via robot-assisted rapid screening approach. The synthesized crystals are initially characterized by X-ray diffraction (XRD) which reveals their layered structures templated by solvent molecules. Specifically, two MA cations and one DMC molecule, in the interlayer, form a hydrogen-bonded $[MA\cdots DMC\cdots MA]^{2+}$ complex that acts as a spacer between the perovskite sheets. Notably, these structures feature relatively short interlayer distances (~5.7–5.9 Å). Other key geometrical aspects

are also discussed in our detailed structural analysis. Furthermore, we measure the steady-state UV-visible absorption and photoluminescence (PL) spectra of these compounds, as well as calculate their electronic band structures by density functional theory (DFT). The results show their similarity to other 2D halide perovskite systems. We then explore the phase stability of these systems. As $MA_3(DMC)Pb_2I_7$ (n=2 iodide) displays relatively better stability among the synthesized compounds, we closely examine its reconstruction into $MAPbI_3$ phase under different conditions: in ambient air, upon heating, and on irradiation with a laser source. In the last section of our study, we demonstrate the reversibility of phase transformations involving solvent-templated 2D Ruddlesden-Popper perovskites owing to the relatively easy intercalation and de-intercalation of DMC molecules between their interlayers. This helps us design a thermochromic system that can withstand 25 cycles of switching between two colored states.

RESULTS AND DISCUSSION

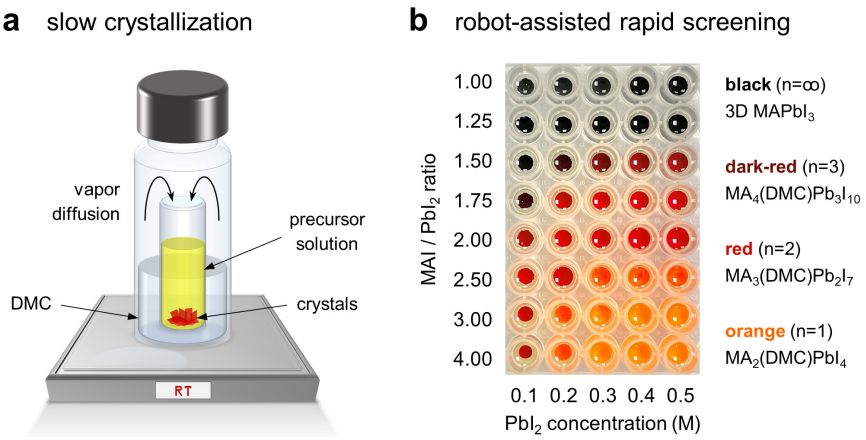

Figure 1. (a) Schematics of antisolvent vapor-assisted crystallization (AVC) method for the growth of solvent-templated 2D Ruddlesden-Popper perovskite crystals. (b) Robot-assisted rapid screening of reaction conditions for $MA_2(DMC)PbI_4$ (n=1 iodide, orange), $MA_3(DMC)Pb_2I_7$ (n=2 iodide, red), and $MA_4(DMC)Pb_3I_{10}$ (n=3 iodide, dark-red) phases.

Synthesis. We synthesized new solvent-templated 2D Ruddlesden-Popper perovskites by two different approaches (Figure S1). First method involved conventional antisolvent vapor-assisted crystallization (AVC) where dimethyl carbonate (DMC) slowly diffused into a perovskite precursor solution containing MAI/PbI_2 in γ-butyrolactone (GBL) or $MABr/PbBr_2$ in *N*,*N*-

dimethylformamide (DMF) (Figure 1a). To determine the conditions for the crystallization of iodides, rapid screening of a 2D map of different MAI and PbI_2 concentrations in the solution was conducted using an Opentrons OT-2 liquid-handling robotic system (see Figure 1b and Figure S2). Specifically, we prepared an 8×5 matrix plate with 40 various solution combinations and then, by adding the excess amount of DMC to each well, we were able to precipitate the target phases in those wells. The resulting precipitates varied around several microns in size (Figure S3). This also demonstrates the relatively easy formability of these materials at room temperature. Next, the optimal MAI and PbI_2 concentrations were retrieved to slowly grow larger crystals of solvent-templated 2D Ruddlesden-Popper perovskites by AVC method. The MAI/PbI_2 and MABr/$PbBr_2$ concentrations in their respective solvents were set at 1.2/0.3 M (4:1), 0.6/0.3 M (2:1), 0.45/0.3 M (1.5:1), and 0.75/0.25 M (3:1) to achieve mm-sized crystals of $MA_2(DMC)PbI_4$ (n=1 iodide), $MA_3(DMC)Pb_2I_7$ (n=2 iodide), $MA_4(DMC)Pb_3I_{10}$ (n=3 iodide), and $MA_3(DMC)Pb_2Br_7$ (n=2 bromide), respectively, within 1–2 weeks. The corresponding crystals showed distinct orange, red, dark-red, and yellow colors (Figure 2a).

In an alternative crystallization approach, we prepared MAI/PbI_2 and MABr/$PbBr_2$ suspensions in DMC and dissolved the precursor mixtures by bubbling methylamine (CH_3NH_2) gas through these suspensions under continuous stirring (Figure S1b).[34,35] The obtained two-layered liquid systems were allowed to undergo slow crystallization over 3–5 days. Analogously, by carefully optimizing the precursor amounts, we were able to crystallize $MA_3(DMC)Pb_2I_7$ (n=2 iodide), $MA_4(DMC)Pb_3I_{10}$ (n=3 iodide), and $MA_3(DMC)Pb_2Br_7$ (n=2 bromide) phases (see Supporting Information for details). We believe that the crystallization is achieved owing to the slow release of methylamine gas by the obtained liquid systems, allowing DMC molecules gradually template the growth 2D perovskite phases.

It is worth mentioning that we were unable to isolate phases with higher *n*-values (n>3) in neither iodides nor bromides. This is consistent with the general perception of the difficulty of synthesizing those phases.[10,36] In case of bromides, we only occasionally observed the formation of n=3 phase along with n=2 and $MAPbBr_3$ phases when the MABr/$PbBr_2$ ratio was reduced to 2:1 and below. On the other hand, the synthesis of n=1 phases also seemed to be challenging. We were only able to crystallize $MA_2(DMC)PbI_4$ (n=1 iodide) phase by AVC method at high (≥3:1) MAI/PbI_2 ratios, while the alternative approach using methylamine gas did consistently result in

n=2 phase. We also noticed that the synthesized n=1 iodide crystals are unstable at ambient conditions. These observations suggest that n=2 could be thermodynamically the most stable phase in both iodides and bromides.

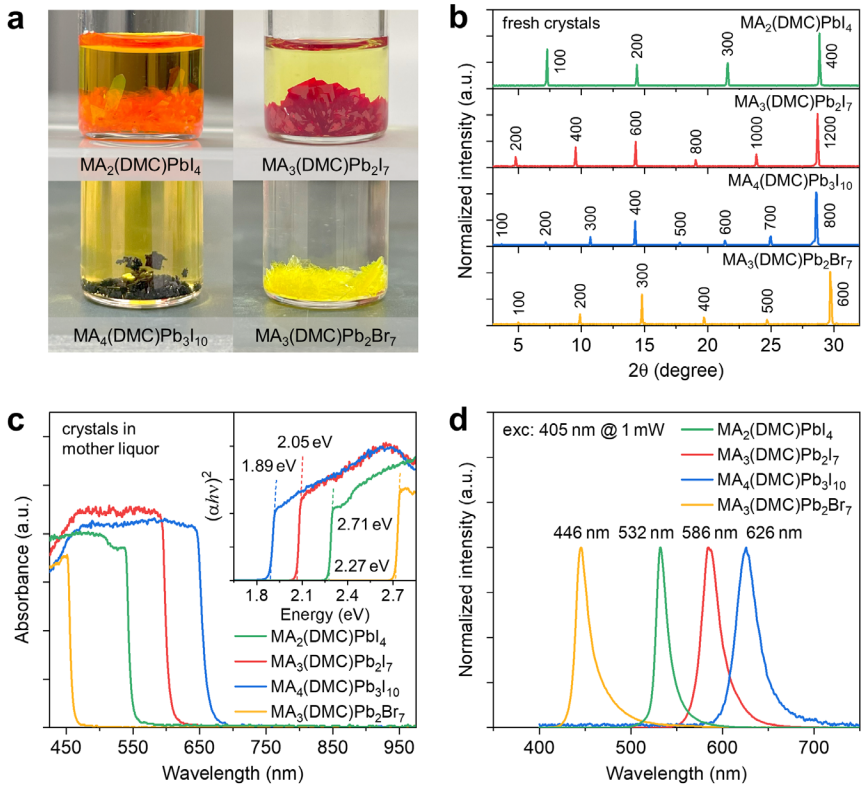

Figure 2. (a) Optical images, (b) 2θ-XRD patterns, (c) UV-visible absorption spectra, and (d) PL emission spectra of solvent-templated 2D Ruddlesden-Popper perovskite crystals: $MA_2(DMC)PbI_4$ (n=1 iodide, green lines), $MA_3(DMC)Pb_2I_7$ (n=2 iodide, red lines), $MA_4(DMC)Pb_3I_{10}$ (n=3 iodide, blue lines), and $MA_3(DMC)Pb_2Br_7$ (n=2 bromide, yellow lines). Inset of panel (c): corresponding Tauc plots showing the bandgap values of these crystals.

Characterization. We next performed characterization of solvent-templated 2D Ruddlesden-Popper perovskites. The 2θ-XRD patterns of as-synthesized crystals showed their preferential orientation along (h00) crystallographic planes (Figure 2b). The diffraction peaks matched well with the calculated patterns (Figure S4a). We observed one, two, and three characteristic low-angle peaks below 2θ~14° for n=1, n=2, and n=3 phases, respectively, confirming the absence of other phases in the grown crystals. The d-spacing values for $MA_2(DMC)PbI_4$ (n=1 iodide),

$MA_3(DMC)Pb_2I_7$ (n=2 iodide), $MA_4(DMC)Pb_3I_{10}$ (n=3 iodide), and $MA_3(DMC)Pb_2Br_7$ (n=2 bromide) were estimated as 12.3 Å, 18.5 Å, 24.8 Å, and 17.9 Å, respectively.

The UV-visible absorption spectra of as-synthesized crystals in their mother liquor showed the bandgap (E_g) values of 2.27 eV, 2.05 eV, 1.89 eV, and 2.71 eV for $MA_2(DMC)PbI_4$ (n=1 iodide), $MA_3(DMC)Pb_2I_7$ (n=2 iodide), $MA_4(DMC)Pb_3I_{10}$ (n=3 iodide), and $MA_3(DMC)Pb_2Br_7$ (n=2 bromide), respectively (Figure 2c). These values are slightly smaller than for BA- or PEA-based RP perovskites.[7] For instance, BA_2PbI_4 (n=1), $MA(BA)_2Pb_2I_7$ (n=2) and $MA_2(BA)_2Pb_3I_{10}$ (n=3) crystals have bandgap values of 2.43 eV, 2.17 eV, and 2.03 eV, respectively (Table S1). However, the values were found to be close to the bandgaps of DJ perovskites.[8] For instance, $(3AMP)PbI_4$ (n=1), $MA(3AMP)Pb_2I_7$ (n=2), and $MA_2(3AMP)Pb_3I_{10}$ (n=3) (where 3AMP is 3-(aminomethyl)piperidinium) crystals have bandgap values of 2.23 eV, 2.02 eV, and 1.92 eV, respectively (Table S1). Notably, we also observed the presence of excitonic peaks in the absorption spectra of solvent-templated 2D Ruddlesden-Popper perovskites for their pulverized crystals in mother liquor (Figure S4b). Next, we measured the photoluminescence (PL) spectra of as-synthesized fresh crystals using a 405-nm excitation source at 1 mW (Figure 2d). The PL peak positions for $MA_2(DMC)PbI_4$ (n=1 iodide), $MA_3(DMC)Pb_2I_7$ (n=2 iodide), $MA_4(DMC)Pb_3I_{10}$ (n=3 iodide), and $MA_3(DMC)Pb_2Br_7$ (n=2 bromide) crystals were found at 532 nm (2.33 eV), 586 nm (2.12 eV), 626 nm (1.98 eV), and 446 nm (2.78 eV), respectively (Figure 2d). Meanwhile, their full-width-at-half-maximum (FWHM) values were estimated as 14 nm, 24 nm, 28 nm, and 18 nm, respectively, showing signal broadening with the layer thickness (*n*) (Figure S4c).

Other Solvent-Templated Systems. DMC molecule has three O-atoms that can potentially coordinate Pb and form H-bonds with MA cation (Figure S5a). However, unlike ethylene carbonate (EC) and propylene carbonate (PC), it has a lower propensity to dissolve perovskites. We believe that this interplay between the ability to form non-covalent interactions with perovskite precursors and yet not dissolve them enables the templated growth of 2D perovskites.

To further expand the library of solvents that can template 2D halide perovskites, we tried the following liquids with structural motifs similar to DMC: diethyl carbonate (DEC), diethyl oxalate (DEO), ethyl acetate (EtAc), and methyl methacrylate (MMA) (Figure S5a). We prepared MAI/PbI_2 solutions in GBL with molar ratios varied between 2:1 and 3:1. By adding the excess

amount of the respective solvents to these solutions, we were able to precipitate dark-red solids in each case. Interestingly, these materials were found to be more unstable than their DMC-templated counterparts, instantly turning black at ambient conditions. However, we were able to record the steady-state UV-visible absorption and photoluminescence (PL) spectra of these solids in their mother liquor (Figure S5b). The absorption edges for DEC-, DEO-, EtAc-, and MMA-templated solids were found near 670 nm (1.85 eV), 713 nm (1.74 eV), 684 nm (1.81 eV), and 713 nm (1.74 eV), respectively. The PL signals for both DEC- and DEO-templated samples centered around 673 nm (1.84 eV) which is slightly red-shifted relative to the PL peak position of $MA_4(DMC)Pb_3I_{10}$ (n=3, 1.98 eV). Meanwhile, for EtAc- and MMA-templated samples, the PL signal around 670 nm was weak, and the peak at 755 nm, corresponding to $MAPbI_3$, appeared more pronounced. We note that the presence of PL signals below 700 nm might be indicative of the formation of 2D or other low-dimensional perovskite phases.

The 2θ-XRD measurement of the dark-red phase formed by DEC showed similar pattern with $MA_4(DMC)Pb_3I_{10}$ (n=3 iodide) (Figure S5d). The *d*-spacing of the material, presumably $MA_4(DEC)Pb_3I_{10}$ (n=3 iodide), was estimated as 27.2 Å. Meanwhile, the mixture of DMC/DEC solvents (1:1, 1:2, and 1:4 by volume, respectively) resulted in the co-precipitation of bright-red phases with the diffraction patterns similar to $MA_3(DMC)Pb_2I_7$ (n=2 iodide). The *d*-spacing of the DEC-containing phase, presumably $MA_3(DEC)Pb_2I_7$ (n=2 iodide), was estimated as 20.9 Å. The difference between the *d*-spacings of 'n=3' and 'n=2' phases was found to be around 6.3 Å which matches with the thickness of one octahedral layer. This observation suggests that DEC likely forms 2D perovskite phases similar to those formed by DMC.

Table 1. Crystal and refinement data of solvent-templated 2D Ruddlesden-Popper perovskites at 100(2) K: $MA_2(DMC)PbI_4$ (n=1 iodide), $MA_3(DMC)Pb_2I_7$ (n=2 iodide), $MA_4(DMC)Pb_3I_{10}$ (n=3 iodide), and $MA_3(DMC)Pb_2Br_7$ (n=2 bromide).

	$MA_2(DMC)PbI_4$	$MA_3(DMC)Pb_2I_7$	$MA_4(DMC)Pb_3I_{10}$	$MA_3(DMC)Pb_2Br_7$
crystal system	monoclinic	monoclinic	monoclinic	monoclinic
space group	$P2_1/c$	$C2/c$	$P2_1/c$	$P2_1/c$
unit cell dimensions	a = 12.9770(10) Å b = 8.6692(7) Å c = 8.8228(6) Å β = 109.721(4)°	a = 36.9491(11) Å b = 8.7217(2) Å c = 8.8260(3) Å β = 90.5022(12)°	a = 25.163(2) Å b = 8.7261(7) Å c = 8.8035(7) Å β = 99.642(4)°	a = 18.2561(7) Å b = 8.2882(3) Å c = 8.2924(3) Å β = 102.7306(18)°
volume	934.35(12) Å^3	2844.15(14) Å^3	1905.7(3) Å^3	1223.88(8) Å^3
Z	2	4	2	2
density (calculated)	3.089 g/cm^3	3.477 g/cm^3	3.675 g/cm^3	3.148 g/cm^3
index ranges	-21 ≤ h ≤ 21 -14 ≤ k ≤ 14 -14 ≤ l ≤ 14	-56 ≤ h ≤ 57 -12 ≤ k ≤ 13 -13 ≤ l ≤ 13	-34 ≤ h ≤ 34 -12 ≤ k ≤ 12 -12 ≤ l ≤ 11	-28 ≤ h ≤ 25 -12 ≤ k ≤ 12 -12 ≤ l ≤ 12
reflections collected	28520	16300	28923	18153
independent reflections	4329 [R_{int} = 0.1079]	5577 [R_{int} = 0.0413]	5296 [R_{int} = 0.0743]	4897 [R_{int} = 0.0676]
completeness	99.7%	99.6%	100%	99.9%
data / restraints / parameters	4329 / 69 / 102	5577 / 85 / 138	5296 / 99 / 176	4897 / 49 / 138
goodness-of-fit	1.061	1.036	1.077	1.023
final R indices [$I > 2\sigma(I)$]	R_{obs} = 0.0530 wR_{obs} = 0.1230	R_{obs} = 0.0384 wR_{obs} = 0.0946	R_{obs} = 0.0510 wR_{obs} = 0.1080	R_{obs} = 0.0460 wR_{obs} = 0.1143
R indices [all data]	R_{all} = 0.0755 wR_{all} = 0.1348	R_{all} = 0.0472 wR_{all} = 0.0997	R_{all} = 0.0735 wR_{all} = 0.1177	R_{all} = 0.0600 wR_{all} = 0.1239
largest diff. peak and hole	3.62 and –1.99 e·Å^{-3}	2.71 and –1.97 e·Å^{-3}	1.85 and –2.08 e·Å^{-3}	2.41 and –2.44 e·Å^{-3}

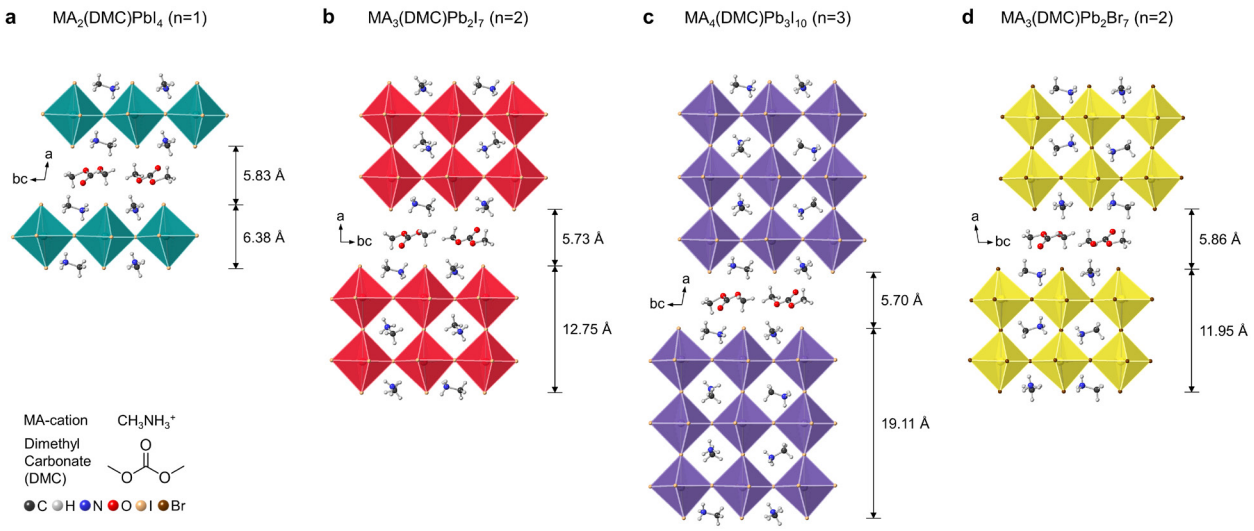

Figure 3. Crystal structures of solvent-templated 2D Ruddlesden-Popper perovskites highlighting their interlayer distances and perovskite slab thicknesses: (a) $MA_2(DMC)PbI_4$ (n=1 iodide), (b)

$MA_3(DMC)Pb_2I_7$ (n=2 iodide), (c) $MA_4(DMC)Pb_3I_{10}$ (n=3 iodide), and (d) $MA_3(DMC)Pb_2Br_7$ (n=2 bromide).

Crystal Structures. To shed more light on the crystal structure of solvent-templated 2D Ruddlesden-Popper perovskites, we performed single crystal XRD analysis. The results revealed the centrosymmetric space group of $P2_1/c$ for $MA_2(DMC)PbI_4$ (n=1 iodide), $MA_4(DMC)Pb_3I_{10}$ (n=3 iodide), $MA_3(DMC)Pb_2Br_7$ (n=2 bromide) and $C2/c$ for $MA_3(DMC)Pb_2I_7$ (n=2 iodide) crystals (Table 1). The structures represent RP phases with the general chemical formula of $MA_{n+1}(DMC)Pb_nX_{3n+1}$ where $[Pb_nX_{3n+1}]^{(n+1)-}$ inorganic slabs are separated by two MA cations and one DMC molecule in the interlayer, and additional (*n-1*) MA cations occupy the octahedral cages inside the inorganic slabs (Figure 3). Consistent with other RP perovskites, the individual $[Pb_nX_{3n+1}]^{(n+1)-}$ slabs in all four structures were found to be staggered by half an octahedron length (½, ½) in *bc*-plane. As expected, the slab thickness varied with the halide size and the layer thickness (*n*), increasing from 6.38 Å for $MA_2(DMC)PbI_4$ (n=1 iodide) to 11.95 Å for $MA_3(DMC)Pb_2Br_7$ (n=2 bromide) to 12.75 Å for $MA_3(DMC)Pb_2I_7$ (n=2 iodide) and 19.11 Å for $MA_4(DMC)Pb_3I_{10}$ (n=3 iodide). Interestingly, the interlayer distance, *i.e.* the distance between the slabs, were found to be around 5.70–5.73 Å for $MA_3(DMC)Pb_2I_7$ (n=2 iodide) and $MA_4(DMC)Pb_3I_{10}$ (n=3 iodide) phases and 5.83–5.86 Å for $MA_2(DMC)PbI_4$ (n=1 iodide) and $MA_3(DMC)Pb_2Br_7$ (n=2 bromide) phases. These distances are shorter than those in archetypal RP perovskites based on PEA and BA cations, but comparable with those in iso-propylammonium (IPA)- and ethylammonium (EA)-based RP perovskites (Table S1).[14,37] On the other hand, methylhydrazinium (MHy)- and cesium-based RP perovskites,[11,38] as well as some DJ,[8,39] ACI,[40,41] and corrugated perovskites[42–44] exhibit even shorter interlayer distances of about 3–4 Å. Yet, to the best of our knowledge, the structures presented here feature one of the narrowest interlayers among reported solvent-incorporated 2D halide perovskites.[17,26] Short interlayer distances can be of great importance for efficient charge transfer between the semiconducting perovskite sheets.

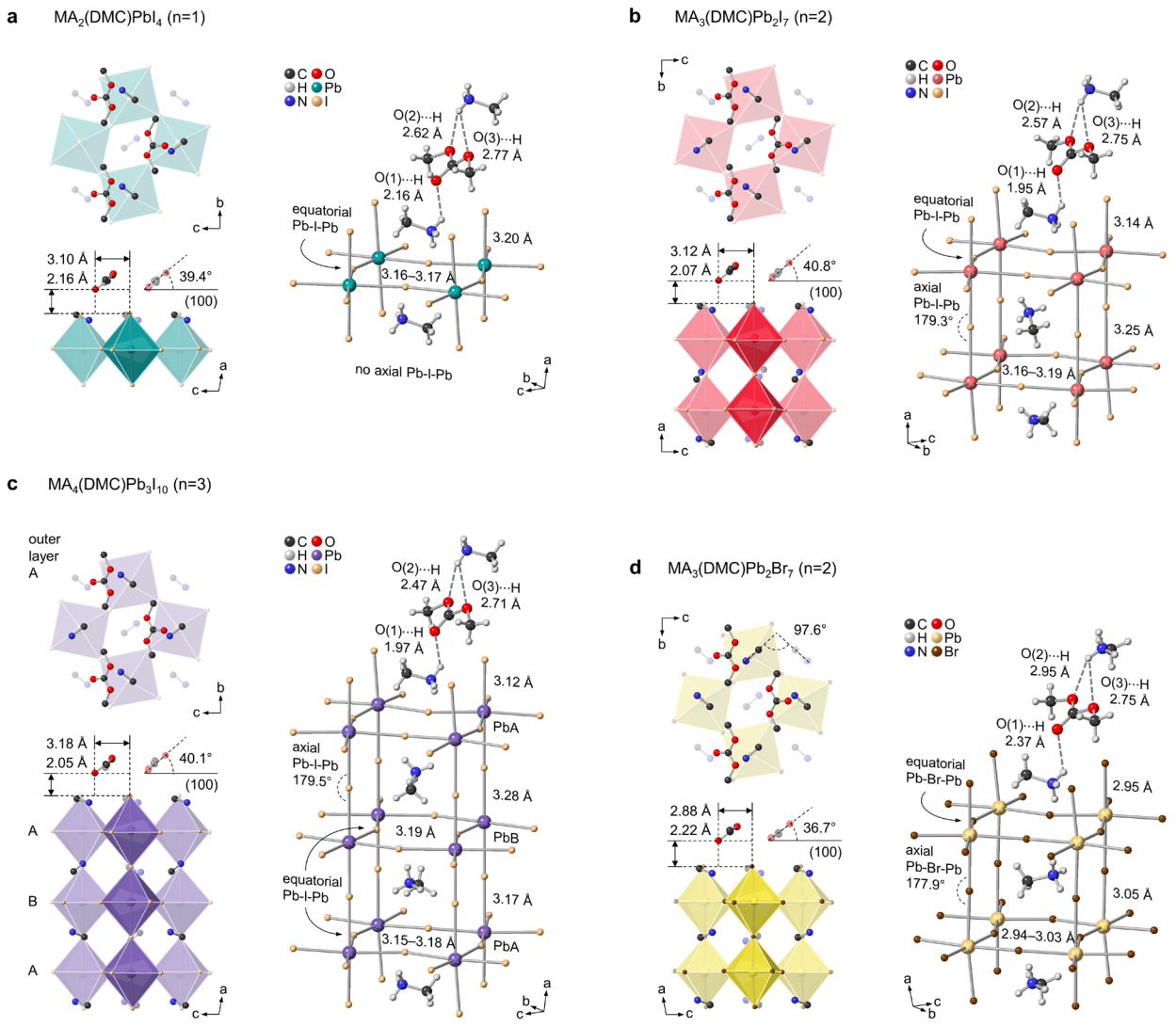

Figure 4. Detailed crystal structure representations of solvent-templated 2D Ruddlesden-Popper perovskites highlighting the orientations of organic moieties and the key geometric parameters such as bond lengths and angles: (a) $MA_2(DMC)PbI_4$ (n=1 iodide), (b) $MA_3(DMC)Pb_2I_7$ (n=2 iodide), (c) $MA_4(DMC)Pb_3I_{10}$ (n=3 iodide), and (d) $MA_3(DMC)Pb_2Br_7$ (n=2 bromide).

To understand how DMC molecules and MA cations pack in these structures, we took a closer look at their interlayers. Figure 3 shows that, in all four structures, a DMC molecule occupies a tight space between two inorganic slabs and two MA cations residing in the pockets of those slabs. The structures are primarily held by the electrostatic interactions between MA cations and negatively charged $[Pb_nX_{3n+1}]^{(n+1)-}$ inorganic slabs, as well as the hydrogen bonding between the O-atoms of DMC molecule and the H-atoms of NH_3-group of MA cations in the interlayer (see

ball-and-stick representations in Figure 4). In each structure, we have identified three different H-bonds: O(1)···H, O(2)···H, and O(3)···H. The optimized distance of the shortest one, that is O(1)···H, correlates well with the interlayer distance, increasing by *ca*. 10 and 20% from around 1.95–1.97 Å for $MA_3(DMC)Pb_2I_7$ (n=2 iodide) and $MA_4(DMC)Pb_3I_{10}$ (n=3 iodide) to 2.16 Å for $MA_2(DMC)PbI_4$ (n=1 iodide) and 2.37 Å for $MA_3(DMC)Pb_2Br_7$ (n=2 bromide), respectively (Table S2). Meanwhile, another key parameter of H-bonding, that is O(1)···H–N angle, showed the opposite trend decreasing from around 129–132° to 117° and 109°, respectively. Such differences are indicative of DMC molecules having weaker interactions with MA cations in the latter two structures. This also results in relatively reduced phase stability of $MA_2(DMC)PbI_4$ (n=1 iodide) and $MA_3(DMC)Pb_2Br_7$ (n=2 bromide) phases compared to $MA_3(DMC)Pb_2I_7$ (n=2 iodide) and $MA_4(DMC)Pb_3I_{10}$ (n=3 iodide) phases, as will be demonstrated in the following sections.

Further structural analysis revealed that DMC molecules are tilted in the interlayer, making an angle of around 39.4–40.8° and 36.7° with the (100) planes of the iodide and the bromide crystals, respectively (see side-view representations in Figure 4). This is probably to match the lattice parameter of the perovskite slabs. We also noticed that, in the bromide, DMC molecules are slightly shifted in *bc*-plane towards the apical Br-atoms. Another major difference between the iodide and bromide structures is in the orientation of MA cations in the interlayer. Specifically, the axes of two MA cations above and below a DMC molecule make an angle of 0° (180°) in the iodide phases and 82.4° (97.6°) in the bromide phase (see top-view representations in Figure 4).

Overall, we observed that two MA cations and one DMC molecule in the interlayers of these structures form hydrogen-bonded $[MA\cdots DMC\cdots MA]^{2+}$ complexes that act as spacers between the perovskite sheets. We believe that the presence of three non-covalently bound organic moieties makes these structures relatively unstable compared to RP and DJ perovskites which, respectively, have only two and one organic moiety in their interlayers. While the (in)stability of solvent-templated systems likely originates from their interlayers, the optical and electronic properties mainly depend on the structural features of the inorganic slabs,[45–48] which we discuss below.

Table 2. The key parameters describing the distortions of octahedral framework and individual octahedra in solvent-templated 2D Ruddlesden-Popper perovskites: $MA_2(DMC)PbI_4$ (n=1 iodide), $MA_3(DMC)Pb_2I_7$ (n=2 iodide), $MA_4(DMC)Pb_3I_{10}$ (n=3 iodide), and $MA_3(DMC)Pb_2Br_7$ (n=2 bromide).

		∠Pb-X-Pb axial	∠Pb-X-Pb equatorial (avg.)	Pb-X length axial (outer/inner)	Pb-X length equatorial (avg.)	distortion index (*D*)	bond angle variance (σ^2)
$MA_2(DMC)PbI_4$ (n=1)		–	155.3°	3.20 Å	3.17 Å	0.0052	4.07
$MA_3(DMC)Pb_2I_7$ (n=2)		179.3°	155.9°	3.14 / 3.25 Å	3.17 Å	0.0080	6.59
$MA_4(DMC)Pb_3I_{10}$ (n=3)	A	179.5°	157.3°	3.12 / 3.28 Å	3.16 Å	0.0115	7.58
	B		152.9°	3.17 Å	3.19 Å	0.0027	0.10
$MA_3(DMC)Pb_2Br_7$ (n=2)		177.9°	157.2°	2.95 / 3.05 Å	2.99 Å	0.0121	10.57

To assess the deviation of inorganic slabs from an ideal octahedral framework, *i.e.* the degree of inter-octahedral distortion, we first evaluated the axial and equatorial Pb-X-Pb angles in each structure (see ball-and-stick representations in Figure 4). While $MA_2(DMC)PbI_4$ (n=1 iodide) has no axial Pb-X-Pb angles, other three structures showed nearly ideal angles (~180°). On the other hand, the equatorial Pb-X-Pb angles in all structures showed a noticeable deviation from an ideal case, falling within the range of 150–160° (Table 2). Interestingly, both the axial and the equatorial angles in our structures were found to be close to those in tetragonal $MAPbI_3$, suggesting that these two parameters are related to the geometry of MA cation.[49] Next, we compared the Pb-X bond lengths in these structures. We noticed that, for n=2–3 phases, the axial Pb-X bonds in the outer and inner sides of $[Pb_nX_{3n+1}]^{(n+1)-}$ slabs are, respectively, shortened and elongated as compared to the equatorial Pb-X bonds. For instance, the Pb-I bond lengths in $MA_3(DMC)Pb_2I_7$ (n=2 iodide) are 3.14 Å, 3.25 Å, and ~3.17 Å for outer axial, inner axial, and average equatorial bonds, respectively. This might be because the inner sides of $[Pb_nX_{3n+1}]^{(n+1)-}$ slabs need to accommodate the MA cations, whereas the Pb-X bonds at the surface of the slabs are compressed by the interlayer to balance the expansion of octahedral cages.[16,50]

The distortion of individual octahedra, *i.e.* the intra-octahedral distortion, is better illustrated by two key parameters: the distortion index (*D*) and the bond angle variance (σ^2).[51,52] These parameters, which are expressed by equations 1 and 2, respectively, define the deviation of Pb-X bond lengths (l_i) from the average value (l_{avg}) and the deviation of X-Pb-X angles (θ_i) from 90°:

$$D = \frac{1}{6}\sum_{i}^{6}\frac{|l_i - l_{avg}|}{l_{avg}} \quad (1)$$

$$\sigma^2 = \frac{1}{11}\sum_{i}^{12}(\theta_i - 90)^2 \quad (2)$$

As seen from Table 2, $MA_3(DMC)Pb_2Br_7$ (n=2 bromide) exhibits the largest degree of intra-octahedral distortion, with its both D and σ^2 parameters being the greatest among the four structures. Interestingly, for the iodide phases, the distortion appears to increase with the n value, similar to that in their BA- and PEA-based analogs (Table S3). It is worth mentioning that, in case of $MA_4(DMC)Pb_3I_{10}$ (n=3 iodide), the inorganic slab adopts an A–B–A stacking pattern with outer (A) and inner (B) layers displaying different degrees of intra-octahedral distortion. Namely, the outer layer (A) shows a distortion comparable to that of $MA_3(DMC)Pb_2Br_7$ (n=2 bromide), while the octahedra in the inner layer (B) are nearly ideal with marginal D and σ^2 values. This suggests that the intra-octahedral distortions might mainly arise due to geometric (e.g. lattice) mismatches between the DMC molecules and the $[MA_{n+1}Pb_nX_{3n+1}]$ framework.[33]

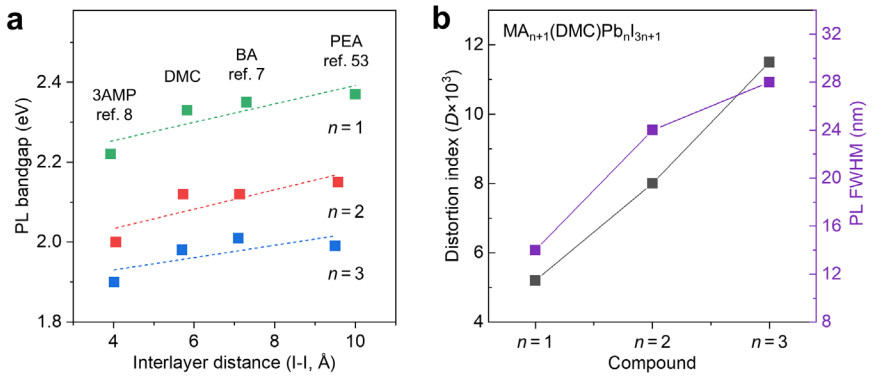

Figure 5. (a) Correlation of the photoluminescence (PL) bandgap with the interlayer distance measured between two adjacent inorganic slabs in different types of 2D iodide perovskite structures (3AMP is 3-(aminomethyl)piperidinium,[8] BA is butylammonium,[7] and PEA is phenethylammonium[53]). (b) Correlation of the full-width-at-half-maximum (FWHM) value of the PL peak and the distortion index (D) with the layer thickness (n) of $MA_{n+1}(DMC)Pb_nI_{3n+1}$ (n=1,2,3) phases.

Comparing these structural features and their relation to optical properties in different 2D perovskite systems, we noticed that the photoluminescence (PL) bandgap increases with the interlayer distance between the inorganic slabs (Figure 5a). With the distance of about 5.8 Å, the PL bandgaps of solvent-templated 2D Ruddlesden-Popper perovskites situate between the bandgaps of 3AMP- and BA-based 2D perovskites which, respectively, display interlayer distances of about 4.0 and 7.2 Å. On the other hand, it has also previously been reported that broad PL emission spectra in halide perovskites may originate from their structural deformations.[46–48] As the Pb-X-Pb angles across our compounds were found to be nearly similar, we believe that the observed PL emission broadening in the iodides with the layer thickness (*n*) primarily stems from their increasing distortion index (*D*) in the series (see Figure 2d and Figure 5b).

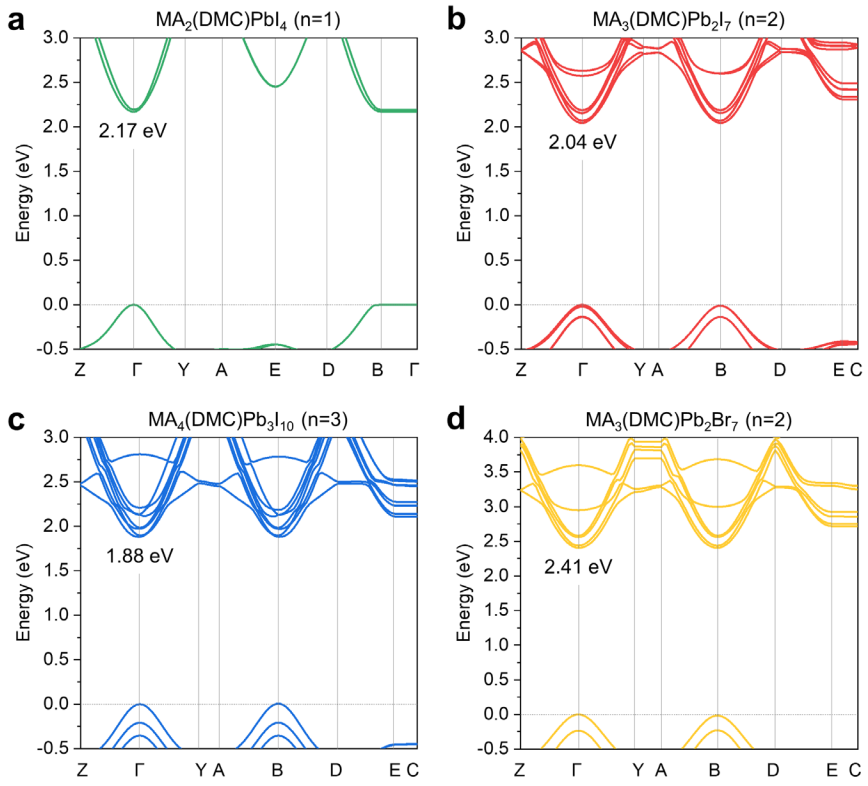

Figure 6. Electronic band structures of solvent-templated 2D Ruddlesden-Popper perovskites: (a) $MA_2(DMC)PbI_4$ (n=1 iodide), (b) $MA_3(DMC)Pb_2I_7$ (n=2 iodide), (c) $MA_4(DMC)Pb_3I_{10}$ (n=3 iodide), and (d) $MA_3(DMC)Pb_2Br_7$ (n=2 bromide). The DFT calculations were performed at GGA/PBE+vdW level of theory.

Table 3. The interlayer and optimized H-bond distances, H-bond strengths, experimental bandgaps, and DFT calculation results for solvent-templated 2D Ruddlesden-Popper perovskites: $MA_2(DMC)PbI_4$ (n=1 iodide), $MA_3(DMC)Pb_2I_7$ (n=2 iodide), $MA_4(DMC)Pb_3I_{10}$ (n=3 iodide), and $MA_3(DMC)Pb_2Br_7$ (n=2 bromide); where m_e and m_h are the electron and hole effective masses, and m_0 is the free electron mass.

	interlayer distance	O(1)···H distance	H-bond strength (eV)	in-plane m_e, m_h (calc.)	bandgap (calc.)	bandgap (exp.)
$MA_2(DMC)PbI_4$ (n=1)	5.83 Å	2.16 Å	0.30 eV	0.25 / 0.28 m_0	2.17 eV	2.27 eV
$MA_3(DMC)Pb_2I_7$ (n=2)	5.73 Å	1.95 Å	0.42 eV	0.22 / 0.26 m_0	2.04 eV	2.05 eV
$MA_4(DMC)Pb_3I_{10}$ (n=3)	5.70 Å	1.97 Å	0.41 eV	0.33 / 0.23 m_0	1.88 eV	1.89 eV
$MA_3(DMC)Pb_2Br_7$ (n=2)	5.86 Å	2.37 Å	0.21 eV	0.33 / 0.29 m_0	2.41 eV	2.71 eV

Electronic Structures. We further performed the density functional theory (DFT) calculations of the electronic band structures using the generalized gradient approximation (GGA) at the Perdew–Burke–Ernzerhof (PBE) level with van der Waals (vdW) interactions (see Figure 6 and Figure S6). The results revealed that all structures are direct-bandgap semiconductors exhibiting a clear 2D electronic structure with dispersive bands in the layer direction (i.e. in-plane: Γ→Y and Γ→Z) and flat bands in the stacking direction (i.e. out-of-plane: Γ→B). In the iodide phases, the calculated bandgaps closely match with the experimental values (Table 3). However, for $MA_3(DMC)Pb_2Br_7$ (n=2 bromide), the calculated bandgap was slightly smaller than the experimental one, which is consistent with the known tendency of GGA/PBE method to underestimate bandgaps of bromide perovskites. The projected densities of states (PDOS) show that, in all four structures, the dominant contribution to the valence and conduction bands originates from Pb and X orbitals (Figure S7). Both MA cations and DMC molecules, as expected for halide perovskites, have no direct contribution to the band structure.

In the layer direction of these 2D perovskite structures, the calculated effective masses for both holes and electrons fall within the range of 0.2–0.4 m_0 (Table 3). In the stacking direction, both the conduction and valence bands are notably flat. While it is worth mentioning that, for holes, the calculated out-of-plane effective masses are only one order of magnitude heavier than their in-plane counterparts. This can be attributed to the electronic interaction between the $[Pb_nX_{3n+1}]^{(n+1)-}$ inorganic slabs induced by the decreased interlayer distances in these structures.

Furthermore, the calculated formation energies for all four structures were determined to be negative, confirming their formability. Specifically, the formation energy for $MA_3(DMC)Pb_2Br_7$ (n=2 bromide) was calculated as -2.23 eV per unit $PbBr_2$. Meanwhile, within the iodide phases, the formation energy per unit PbI_2 increased with the layer thickness (*n*) from -2.75 eV for $MA_2(DMC)PbI_4$ (n=1) to -1.88 eV for $MA_3(DMC)Pb_2I_7$ (n=2) and -1.58 eV for $MA_4(DMC)Pb_3I_{10}$ (n=3). While this observed trend aligns with previous theoretical calculations for 2D perovskites in the literature,[54] some experimental studies have indicated the variation between the formation enthalpies of odd- and even- numbered 2D perovskites, with the lowest values shown for n=2 and n=4 phases.[36] Therefore, we highlight the importance of calorimetric measurements to more accurately estimate the formation energies in solvent-templated 2D Ruddlesden-Popper perovskites.

On the other hand, the (in)stability of solvent-templated 2D Ruddlesden-Popper perovskite phases primarily originates from the presence of three non-covalently bound organic moieties in their interlayers. To delve deeper into this aspect, we proceeded to calculate the strengths of H-bonding in these systems. Specifically, the energy associated with the shortest H-bond, *i.e.* O(1)···H, was found to decrease from 0.41-0.42 eV for $MA_3(DMC)Pb_2I_7$ (n=2 iodide) and $MA_4(DMC)Pb_3I_{10}$ (n=3 iodide) phases to 0.30 eV and 0.21 eV for $MA_2(DMC)PbI_4$ (n=1 iodide) and $MA_3(DMC)Pb_2Br_7$ (n=2 bromide) phases, respectively. This trend closely aligns with the observed formability and (in)stability of these materials, indicating the key role of H-bonding in both cases. Future studies could shed light on the influence of defects on the (in)stability of this type of structures.[55]

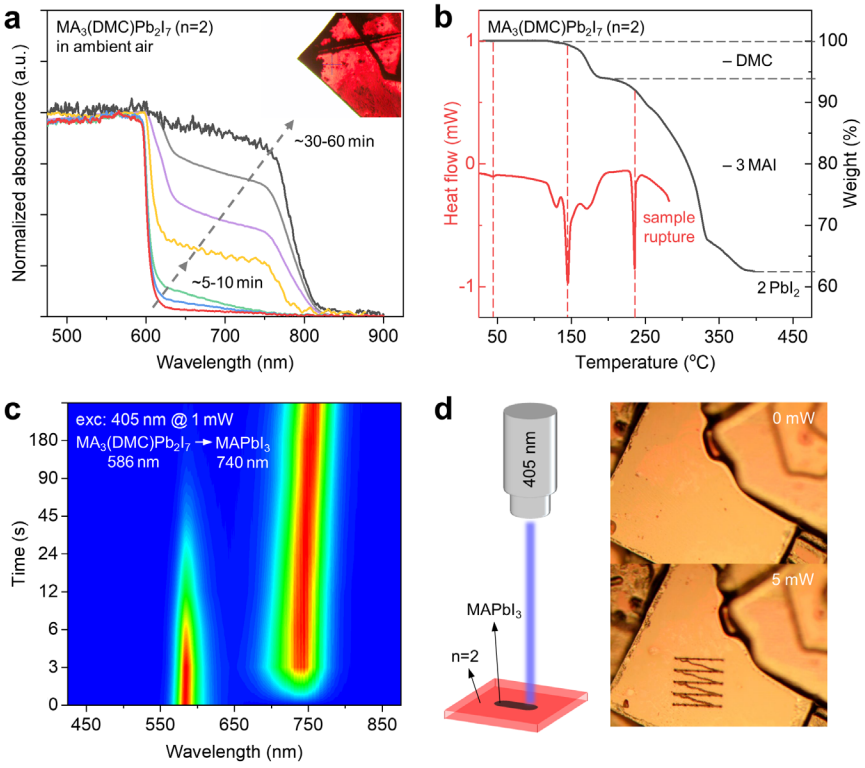

Figure 7. (a) UV-visible absorption spectra of $MA_3(DMC)Pb_2I_7$ (n=2) crystals in ambient air over 1 hour time. (b) TGA and DSC curves of $MA_3(DMC)Pb_2I_7$ (n=2) crystals under inert atmosphere at 5°C/min scanning rate. (c) Photoluminescence (PL) emission spectra of $MA_3(DMC)Pb_2I_7$ (n=2) crystals under a 405-nm laser excitation at 1 mW over 5 mins time. (d) The schematic illustration and optical images of laser direct writing (LDW) of 3D $MAPbI_3$ perovskite phase on the top surface of $MA_3(DMC)Pb_2I_7$ (n=2) crystals.

Transformation into 3D perovskite. Indeed, we noticed that as-synthesized solvent-templated 2D Ruddlesden-Popper perovskites are not phase-stable at ambient conditions (25°C and 70% RH). They reconstruct into 3D $MAPbX_3$ (where X = Br^-, I^-) perovskite phase releasing DMC and MAX as by-products (equation 3). Their relative phase stability correlates well with the optimized H-bond distances and their strengths, reducing in the following order: $MA_3(DMC)Pb_2I_7$ (n=2 iodide) > $MA_4(DMC)Pb_3I_{10}$ (n=3 iodide) > $MA_2(DMC)PbI_4$ (n=1 iodide) ~ $MA_3(DMC)Pb_2Br_7$ (n=2 bromide). In terms of reconstruction time, $MA_3(DMC)Pb_2I_7$ (n=2 iodide) starts turning black within minutes after their extraction from mother liquor. Whereas the reconstruction of $MA_2(DMC)PbI_4$ (n=1 iodide) and $MA_3(DMC)Pb_2Br_7$ (n=2 bromide) is almost instantaneous starting within few seconds in ambient air. Notably, the reconstruction was found to be slower under inert atmosphere suggesting that the process is likely facilitated by humidity or oxygen.

$$MA_{n+1}(DMC)Pb_nX_{3n+1} \rightleftharpoons n\ MAPbX_3 + MAX + DMC \quad (3)$$

Since $MA_3(DMC)Pb_2I_7$ (n=2 iodide) crystals displayed the highest stability among the synthesized phases, we decided to take a closer look at its reconstruction process. First, we confirmed the chemical composition by nuclear magnetic resonance (NMR) spectroscopy. The ^{1}H-NMR spectrum of freshly extracted crystals showed the stoichiometric ratio between MA ($CH_3NH_3^+$) and DMC ($CH_3OCOOCH_3$) (Figure S8a). Next, we observed its transformation into $MAPbI_3$ by UV-vis absorption spectroscopy. We found that the reconstruction process is not homogeneous, and some parts of the crystal transform faster than the other parts, as can be seen from the absorption spectra and the microscopic image in Figure 7a. Overall, the crystal almost fully reconstructed after about an hour which was also confirmed by its XRD (Figure S8b). Meanwhile, thermogravimetric analysis (TGA) and differential scanning calorimetry (DSC) measurements under inert atmosphere (Figure 7b) revealed that thermal reconstruction of $MA_3(DMC)Pb_2I_7$ (n=2) phase proceeds through two main steps: (1) de-intercalation of DMC molecules which starts between 100–150°C and leads to the reconstruction of the n=2 phase into $MAPbI_3$ and MAI, (2) decomposition of $MAPbI_3$ into MAI and PbI_2 between 200–250°C followed by MAI evaporation.

Furthermore, we also observed that laser irradiation facilitates the crystal reconstruction. Namely, exposing the fresh crystals of $MA_3(DMC)Pb_2I_7$ (n=2 iodide) to a 405-nm laser source at 1 mW for over 1.0–1.5 s initiated the formation of $MAPbI_3$ perovskite phase. By tracking the characteristic PL signals from $MA_3(DMC)Pb_2I_7$ (n=2) and $MAPbI_3$ at 586 nm and 740 nm, respectively, we observed a nearly complete conversion of the n=2 iodide crystal into $MAPbI_3$ at the laser focal point after only about 5 mins (Figure 7c). Notably, the signal from $MAPbI_3$ showed a slight red-shift over time which might be indicative of its domain size getting larger by irradiation. Increasing the laser power was found to further facilitate the phase reconstruction. Next, we employed this effect for laser direct writing (LDW) of $MAPbI_3$ perovskite phase on the top surface of $MA_3(DMC)Pb_2I_7$ (n=2) crystals (Figure 7d). We patterned a 5×5 box using a 405-nm laser source at 5 mW with an integration time of 100 ms at each focal point (see microscopic images in Figure 7d). We note that the reconstruction of a 2D phase into $MAPbI_3$ is not an irreversible process. As will be demonstrated in the following section, the reverse transformation can also be realized. Yet,

for crystal samples of solvent-templated 2D perovskites, it is likely that the integrity of their continuous structure cannot be fully restored after their initial reconstruction into $MAPbI_3$.

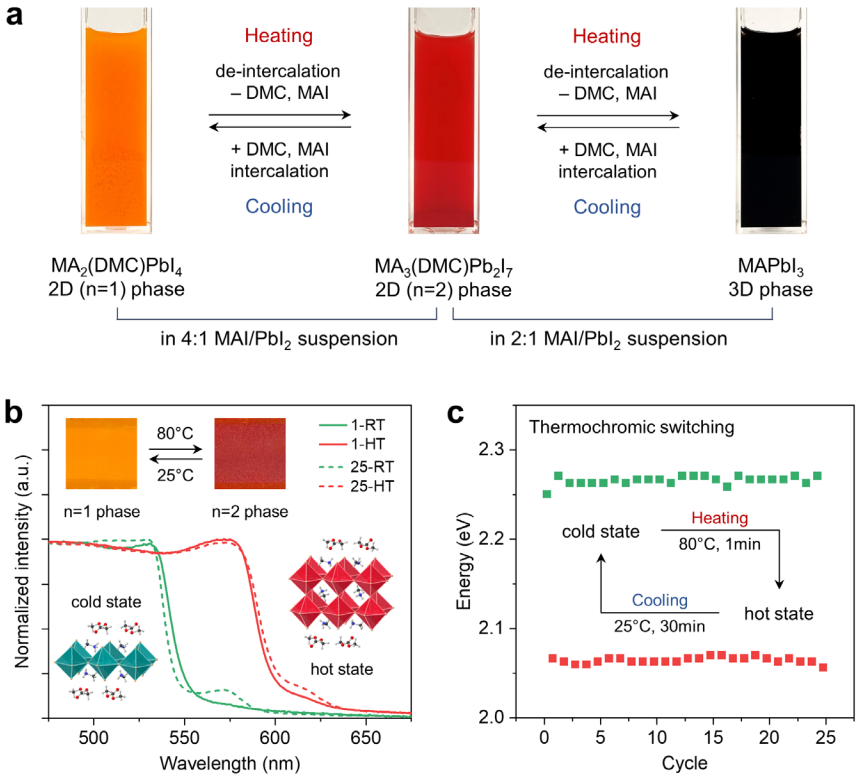

Figure 8. (a) Schematics showing the temperature-induced transformations between $MA_2(DMC)PbI_4$ (n=1, orange color), $MA_3(DMC)Pb_2I_7$ (n=2, red color), and $MAPbI_3$ (3D, black color) phases in perovskite suspensions (inks) prepared from 4:1 and 2:1 molar ratios of MAI/PbI_2. (b) UV-visible absorption spectra of the 4:1 ink sealed between two glass slides: at room temperature (green lines) and after heating at 80°C for 1 min (red lines). Dashed lines represent the corresponding spectra after 25 cycles of switching (heating at 80°C for 1 min and cooling down to room temperature for 30 min). (c) Absorption energy of the 4:1 ink over 25 cycles of switching.

Thermochromic switching. The demonstrated formability and instability of solvent-templated 2D Ruddlesden-Popper perovskites make them ideal candidates for switchable applications.[56,57] We here designed a switchable system based on thermochromic behavior of these materials. By adding the excess amount of DMC to 4:1 and 2:1 MAI/PbI_2 solutions in GBL, we first prepared the suspensions (inks) of $MA_2(DMC)PbI_4$ (n=1, orange color) and $MA_3(DMC)Pb_2I_7$ (n=2, red color) phases, respectively (Figure 8a). We found that heating these suspensions at 80°C for 2 min results in their colors change from orange to red and from red to black, respectively. This is

indicative of temperature-induced transformation of the $MA_2(DMC)PbI_4$ (n=1) phase into $MA_3(DMC)Pb_2I_7$ (n=2), and the $MA_3(DMC)Pb_2I_7$ (n=2) phase into $MAPbI_3$. Interestingly, these reactions were found to be reversible when the suspensions were cooled down to room temperature under continuous stirring over half an hour period. The thermochromic switching behavior between $MA_2(DMC)PbI_4$ (n=1, orange color), $MA_3(DMC)Pb_2I_7$ (n=2, red color), and $MAPbI_3$ (3D, black color) phases were also confirmed by UV-visible absorption spectra before and after heating, as well as after cooling down to room temperature (Figure S9a-b).

Notably, the switching of the 4:1 ink was found to be relatively easier than the switching of the 2:1 ink. Therefore, we next constructed a simple cell composed of the 4:1 ink placed between two glass slides and sealed with a Kapton tape. This cell maintained its thermochromic behavior over 25 cycles of switching (heating at 80°C for 1 min and cooling down to room temperature for 30 min) between its cold (orange) and hot (red) states, represented by $MA_2(DMC)PbI_4$ (n=1) and $MA_3(DMC)Pb_2I_7$ (n=2) phases, respectively (see Supplementary Video 1). This was also confirmed by the corresponding UV-visible absorption spectra (see Figure 8b-c and Figure S9c).

We believe that the switching mechanism involves temperature-induced reversible intercalation/de-intercalation processes between the interlayers of solvent-templated 2D Ruddlesden-Popper perovskites (Figure S9d). More specifically, heating results in the de-intercalation of DMC and MAI molecules from the interlayers and the subsequent condensation, i.e. fusion, of adjacent inorganic slabs. Meanwhile, the negative formation energy of solvent-templated 2D Ruddlesden-Popper perovskites and the concentration gradient present in the inks drive the molecules back into the interlayers when temperature is reduced.

CONCLUSIONS

We successfully synthesized a series of new solvent-templated 2D Ruddlesden-Popper perovskites: $MA_2(DMC)PbI_4$ (n=1 iodide), $MA_3(DMC)Pb_2I_7$ (n=2 iodide), $MA_4(DMC)Pb_3I_{10}$ (n=3 iodide), and $MA_3(DMC)Pb_2Br_7$ (n=2 bromide). Phase-pure crystals were grown using two different crystallization strategies, including antisolvent vapor-assisted crystallization (AVC). The conditions for AVC were determined via robot-assisted rapid screening approach. All four compounds featured layered structures templated by DMC solvent molecules. Methylammonium

(MA) serves as the sole organic cation both within and between the perovskite slabs, while DMC molecules occupy a tight space between MA cations in the interlayer preventing the perovskite sheets from condensing into each other. Our extensive structural analysis revealed that hydrogen bonds between the O-atoms of DMC molecules and H-atoms of NH_3-group of MA cations in the interlayer play a critical role in stabilizing these structures. The resulting $[MA\cdots DMC\cdots MA]^{2+}$ complexes act as spacers, separating the perovskite sheets. Despite comprising three individual species, these interlayers are one of the narrowest (~5.7–5.9 Å) in solvent-incorporated 2D halide perovskites reported so far, which is an essential factor for efficient charge transfer between the semiconducting perovskite sheets.

Furthermore, the synthesized crystals display similar UV-vis absorption and PL spectra as reported 2D halide perovskites. The bandgaps for $MA_2(DMC)Pb_2I_7$ (n=1 iodide), $MA_3(DMC)Pb_2I_7$ (n=2 iodide), $MA_4(DMC)Pb_3I_{10}$ (n=3 iodide), and $MA_3(DMC)Pb_2Br_7$ (n=2 bromide) phases were found to be 2.27 eV, 2.05 eV, 1.89 eV, and 2.71 eV, respectively. The DFT calculations showed their direct-bandgap nature with dispersive bands in the layer direction. Notably, in the iodide phases, the FWHM values of PL signals increased with the layer thickness (*n*), likely associated with the increasing distortion index (*D*) of individual octahedra in this series.

Moreover, the phase stability of the synthesized solvent-templated 2D Ruddlesden-Popper perovskite crystals was found to correlate well with the optimized H-bond distances in them and their strengths, reducing in the following order: $MA_3(DMC)Pb_2I_7$ (n=2 iodide) > $MA_4(DMC)Pb_3I_{10}$ (n=3 iodide) > $MA_2(DMC)PbI_4$ (n=1 iodide) ~ $MA_3(DMC)Pb_2Br_7$ (n=2 bromide). Upon close examination of $MA_3(DMC)Pb_2I_7$ (n=2 iodide) phase by XRD, TGA, DSC, UV-visible absorption and PL spectroscopies, we confirmed its phase reconstruction into $MAPbI_3$ in ambient air. Additionally, irradiation with a laser source was found to facilitate the reconstruction process, enabling a laser direct writing (LDW) of $MAPbI_3$ perovskite phase on the top surface of $MA_3(DMC)Pb_2I_7$ (n=2 iodide) crystals.

We also demonstrated that such transformations of solvent-templated 2D Ruddlesden-Popper perovskites are, in fact, reversible processes. We designed a switchable system based on thermochromic behavior of these materials. A simple cell composed of the 4:1 MAI/PbI_2 ink was successfully switched for 25 cycles between its cold (orange) and hot (red) states, represented by

$MA_2(DMC)PbI_4$ (n=1) and $MA_3(DMC)Pb_2I_7$ (n=2) phases, respectively. We believe that the relatively easy formation and reconstruction of these materials make them ideal candidates for switchable applications.

In conclusion, we anticipate that these new solvent-templated 2D Ruddlesden-Popper perovskites, with their unique structures, will offer valuable insights into structure-property relationships in 2D halide perovskites. Moreover, we hope they will guide the perovskite community in exploring new systems based on solvent-incorporation effect. An intriguing avenue for future research also lies in extending these design principles to incorporate solid phases, as well as translating them into lead-free systems such as layered double perovskites.

EXPERIMENTAL SECTION

Chemicals. Methylammonium iodide (MAI) and methylammonium bromide (MABr) were purchased from Greatcell Solar Ltd. Lead iodide (PbI_2) and lead bromide ($PbBr_2$) were purchased from Tokyo Chemical Industries Co. Ltd. Methylamine solution (33 wt.% in absolute ethanol), γ-butyrolactone (GBL), *N*,*N*-dimethylformamide (DMF), dimethyl carbonate (DMC), diethyl carbonate (DEC), ethyl acetate (EtAc) were purchased from Sigma Aldrich. Diethyl oxalate (DEO) and methyl metacrylate (MMA) were purchased from Alfa Aesar. Deuterated dimethyl sulfoxide (DMSO-d_6) was purchased from Cambridge Isotope Laboratories, Inc. All chemicals were used as received without further purification.

Synthesis. For antisolvent vapor-assisted crystallization (AVC) of $MA_2(DMC)PbX_4$ (n=1 iodide), $MA_3(DMC)Pb_2X_7$ (n=2 iodide), $MA_4(DMC)Pb_3X_{10}$ (n=3 iodide), and $MA_3(DMC)Pb_2Br_7$ (n=2 bromide) phases, 1.2/0.3 M (4:1), 0.6/0.3 M (2:1), 0.45/0.3 M (1.5:1) solutions of MAI/PbI_2 in GBL, and 0.75/0.25 M (3:1) solution of MABr/$PbBr_2$ in DMF, respectively, were prepared and filtered through 0.45-μm PTFE filter. A 0.5 ml of each solution was put into a 4-ml vial, and the vial was placed in a 20-ml vial containing 5 ml DMC. The system was closed and left undisturbed for 1–2 weeks. The obtained crystals were kept in their mother liquor until further characterization. (Note: *see Supporting Information for details of the alternative crystallization approach involving methylamine (CH_3NH_2) gas.*)

Robot-assisted rapid screening. The screening of precursor concentrations for AVC of iodide phases was carried out on polypropylene microplates (96-well, 300-μl, U-bottom, Greiner Bio-One) using an Opentrons OT-2 liquid-handling robotic system. The experiment protocol was written in Python. Opentrons API was used to control the OT-2 pipetting procedures and other hardware modules. Briefly, eight stock solutions containing different MAI/PbI_2 ratios (1.0, 1.25, 1.5, 1.75, 2.0, 2.5, 3.0, and 4.0) with PbI_2 concentration fixed at 0.5 M were prepared. These solutions were mixed with GBL and DMC solvents in various ratios inside microplate wells to precipitate the target $MA_{n+1}(DMC)Pb_nI_{3n+1}$ (n=1,2,3) phases. A total of 40 (8×5) various combinations of different MAI/PbI_2 ratios and PbI_2 concentrations (0.1, 0.2, 0.3, 0.4, and 0.5 M) were explored.

Single crystal X-ray diffraction (XRD). The intensity data were collected at 100(2) K using a Bruker D8 Quest diffractometer with Incoatec microfocus 3.0 Mo source. The structures were solved by Intrinsic Phasing (SHELXTL XT-2014) and refined by full-matrix least squares methods on F^2.[58,59] All non-hydrogen atoms were subjected to anisotropic refinement. The hydrogen atoms were generated geometrically and allowed to ride in their respective parent atoms; they were assigned appropriate isotropic thermal parameters and included in the structure-factor calculations.

Characterizations. The 2θ-XRD patterns of as-synthesized crystals were recorded on a Bruker D8 Advance diffractometer with Cu Kα radiation in the presence of a small amount of mother liquor. The steady-state optical characterization of crystals was performed on a uSight-X micro-spectroscopy system with both the light source and the spectrometer connected to the Nikon Eclipse Ci-S microscope. A halogen lamp and 405-nm laser were used as the excitation sources for UV-visible absorption and photoluminescence (PL) measurements, respectively, while Avantes spectrometer (AvaSpec-ULS2048CL-EVO) was used to record the spectra. The UV-visible absorption was measured using crystals in their mother liquor, both placed on a glass slide, while the PL spectra were recorded from their fresh bare surfaces. The UV-visible absorption measurements of pulverized crystals between two glass slides and perovskite suspensions in cuvettes were carried out on a Shimadzu UV3600 UV-vis-NIR spectrophotometer. The scanning electron microscopy (SEM) images were obtained using JEOL 7600 with an accelerating voltage of 5-15 kV and a working distance of ~8 mm. The proton nuclear magnetic resonance (^{1}H-NMR) spectra were recorded on a Bruker Advance II (400 MHz) spectrometer. The NMR samples were

prepared by dissolving the freshly extracted and dried (with a Kimwipe) crystals of $MA_3(DMC)Pb_2I_7$ (n=2 iodide) in DMSO-d_6. Differential scanning calorimetry (DSC) measurement was carried out on a TA Instruments Q10 DSC. The freshly extracted and dried (with a Kimwipe) crystals of $MA_3(DMC)Pb_2I_7$ (n=2 iodide) (ca. 6.5 mg) were immediately sealed in a standard aluminum pan and analyzed under inert atmosphere in a temperature range from -50°C to 400°C (with a ramp rate of 5°C/min). Thermogravimetric analysis (TGA) was conducted using a TA Instruments Q500 TGA. The freshly extracted and dried (with a Kimwipe) crystals of $MA_3(DMC)Pb_2I_7$ (n=2 iodide) (ca. 15 mg) were analyzed under inert atmosphere in a temperature range from 25°C to 400°C (with a ramp rate of 5°C/min).

Density functional theory (DFT) calculations. The calculations were performed using the projector-augmented wave (PAW) method as implemented in the Vienna Ab initio Simulation Package (VASP) code.[60,61] The generalized gradient approximation (GGA) together with Perdew-Burke-Ernzerhof (PBE) exchange-correlation functional was applied. The van der Waals (vdW) interactions were also considered in the DFT calculations using zero damping method of Grimme (DFT-D3). A uniform grid of 4×4×2 *k*-mesh in the Brillouin zone was employed to optimize the crystal structures of $MA_2(DMC)PbI_4$ (n=1 iodide), and 4×4×1 *k*-mesh for $MA_3(DMC)Pb_2I_7$ (n=2 iodide), $MA_4(DMC)Pb_3I_{10}$ (n=3 iodide), and $MA_3(DMC)Pb_2Br_7$ (n=2 bromide). The energy cutoffs of wave functions were set at 500 eV for the bulk and 450 eV for slabs and interfaces. The atomic positions of all structures were fully relaxed until the Hellman-Feynman forces on each atom were less than 0.01 $eV \cdot Å^{-1}$. The formation energy was calculated by the equation of E (formation) = E (total) – $(n+1)\times E$ (MAI) – $n\times E$ (PbI_2) – E (DMC), where E (formation) is the formation energy, E (total) is the total energy of 2D RP perovskite, E (MAI), E (PbI_2), and E (DMC) are the energies of precursors MAI, PbI_2, and DMC, respectively. The Quantum Theory of Atoms in Molecules (QTAIM) method was employed to study the hydrogen bonds between the H atoms of NH_3^+ and the O atoms of DMC, as implemented in the AIM-UC1 program.[62] The Bond Critical Points (BCPs) for the hydrogen bonds were defined within the range of 2.40 to 3.13 Å.[63] The strength of these hydrogen bonds were further calculated using the equation $\Delta E = -332.34 \times \rho(r_{BCP}) - 1.0661$,[64] where $\rho(r_{BCP})$ represents the charge density at the BCPs.

Thermochromic switching. The switching experiments were conducted using suspensions prepared by adding 5 vol. equivalents of DMC to 0.3 M solutions of $4MAI/PbI_2$ or $2MAI/PbI_2$ in

GBL. A few drops of the obtained suspension (ink) were placed between two glass slides and sealed with a Kapton tape. The typical switching cycle involved heating the cell on a hotplate at 80°C for 1 min and cooling it down to room temperature over about 30 min of time. The UV-visible absorption spectra were collected after each heating and cooling steps.

ASSOCIATED CONTENT

Supporting Information. Materials and Methods. The schematics of two crystallization approaches. The details of robot-assisted rapid screening experiments. The SEM images of powder and crystalline forms of $MA_3(DMC)Pb_2I_7$ (n=2). The calculated 2θ-XRD patterns. The UV-visible absorption spectra of pulverized crystals. The details of experiments on solvent systems similar to DMC. The ^{1}H-NMR spectrum of $MA_3(DMC)Pb_2I_7$ (n=2) in DMSO-d_6. The 2θ-XRD patterns of fresh and aged $MA_3(DMC)Pb_2I_7$ (n=2) crystals. Comparison of bandgap values, interlayer distances, and D and σ^2 parameters between different 2D perovskite phases. The optimized H-bond distances and angles. The electronic band structures with including SOC. Projected density of states (PDOS) plots. (PDF)

Thermochromic switching of the 4:1 MAI/PbI_2 ink at 80°C from the cold (orange) to the hot (red) state. (Video)

Accession Codes. CCDC 2308404–2308407 contain the supplementary crystallographic data for this paper. These data can be obtained free of charge via www.ccdc.cam.ac.uk/data_request/cif, or by emailing data_request@ccdc.cam.ac.uk, or by contacting The Cambridge Crystallographic Data Centre, 12 Union Road, Cambridge CB2 1EZ, UK; fax: +44 1223 336033.

AUTHOR INFORMATION

Notes. Authors declare no conflict of interest.

ACKNOWLEDGEMENTS

This research is supported by the National Research Foundation (NRF) of Singapore under its Competitive Research Program (CRP) (NRF-CRP25-2020-0002). Authors thank Ayat Tassanov from the Department of Chemistry at the Pennsylvania State University (PA 16801,USA) for many fruitful discussions.

REFERENCES

(1) Kojima, A.; Teshima, K.; Shirai, Y.; Miyasaka, T. Organometal Halide Perovskites as Visible-Light Sensitizers for Photovoltaic Cells. *J. Am. Chem. Soc.* **2009**, *131* (17), 6050–6051. https://doi.org/10.1021/ja809598r.

(2) Zhang, W.; Eperon, G. E.; Snaith, H. J. Metal Halide Perovskites for Energy Applications. *Nat. Energy* **2016**, *1* (6), 1–8. https://doi.org/10.1038/nenergy.2016.48.

(3) Wei, H.; Huang, J. Halide Lead Perovskites for Ionizing Radiation Detection. *Nat. Commun.* **2019**, *10* (1), 1066. https://doi.org/10.1038/s41467-019-08981-w.

(4) Xiao, X.; Hu, J.; Tang, S.; Yan, K.; Gao, B.; Chen, H.; Zou, D. Recent Advances in Halide Perovskite Memristors: Materials, Structures, Mechanisms, and Applications. *Adv. Mater. Technol.* **2020**, *5* (6), 1900914. https://doi.org/10.1002/admt.201900914.

(5) Møller, C. K. Crystal Structure and Photoconductivity of Cæsium Plumbohalides. *Nature* **1958**, *182* (4647), 1436–1436. https://doi.org/10.1038/1821436a0.

(6) Weber, D. $CH_3NH_3PbX_3$, Ein Pb(II)-System Mit Kubischer Perowskitstruktur / $CH_3NH_3PbX_3$, a Pb(II)-System with Cubic Perovskite Structure. *Z. Naturforsch. B* **1978**, *33* (12), 1443–1445. https://doi.org/10.1515/znb-1978-1214.

(7) Stoumpos, C. C.; Cao, D. H.; Clark, D. J.; Young, J.; Rondinelli, J. M.; Jang, J. I.; Hupp, J. T.; Kanatzidis, M. G. Ruddlesden–Popper Hybrid Lead Iodide Perovskite 2D Homologous Semiconductors. *Chem. Mater.* **2016**, *28* (8), 2852–2867. https://doi.org/10.1021/acs.chemmater.6b00847.

(8) Mao, L.; Ke, W.; Pedesseau, L.; Wu, Y.; Katan, C.; Even, J.; Wasielewski, M. R.; Stoumpos, C. C.; Kanatzidis, M. G. Hybrid Dion–Jacobson 2D Lead Iodide Perovskites. *J. Am. Chem. Soc.* **2018**, *140* (10), 3775–3783. https://doi.org/10.1021/jacs.8b00542.

(9) Li, X.; Hoffman, J. M.; Kanatzidis, M. G. The 2D Halide Perovskite Rulebook: How the Spacer Influences Everything from the Structure to Optoelectronic Device Efficiency. *Chem. Rev.* **2021**, *121* (4), 2230–2291. https://doi.org/10.1021/acs.chemrev.0c01006.

(10) Stoumpos, C. C.; Soe, C. M. M.; Tsai, H.; Nie, W.; Blancon, J.-C.; Cao, D. H.; Liu, F.; Traoré, B.; Katan, C.; Even, J.; Mohite, A. D.; Kanatzidis, M. G. High Members of the 2D Ruddlesden-Popper Halide Perovskites: Synthesis, Optical Properties, and Solar Cells of $(CH_3(CH_2)_3NH_3)_2(CH_3NH_3)_4Pb_5I_{16}$. *Chem* **2017**, *2* (3), 427–440. https://doi.org/10.1016/j.chempr.2017.02.004.

(11) Li, J.; Yu, Q.; He, Y.; Stoumpos, C. C.; Niu, G.; Trimarchi, G. G.; Guo, H.; Dong, G.; Wang, D.; Wang, L.; Kanatzidis, M. G. $Cs_2PbI_2Cl_2$, All-Inorganic Two-Dimensional Ruddlesden–Popper Mixed Halide Perovskite with Optoelectronic Response. *J. Am. Chem. Soc.* **2018**, *140* (35), 11085–11090. https://doi.org/10.1021/jacs.8b06046.

(12) Rosales, B. A.; Mundt, L. E.; Allen, T. G.; Moore, D. T.; Prince, K. J.; Wolden, C. A.; Rumbles, G.; Schelhas, L. T.; Wheeler, L. M. Reversible Multicolor Chromism in Layered

Formamidinium Metal Halide Perovskites. *Nat. Commun.* **2020**, *11* (1), 5234. https://doi.org/10.1038/s41467-020-19009-z.

(13) Kanwat, A.; Ghosh, B.; Ng, S. E.; Rana, P. J. S.; Lekina, Y.; Hooper, T. J. N.; Yantara, N.; Kovalev, M.; Chaudhary, B.; Kajal, P.; Febriansyah, B.; Tan, Q. Y.; Klein, M.; Shen, Z. X.; Ager, J. W.; Mhaisalkar, S. G.; Mathews, N. Reversible Photochromism in ⟨110⟩ Oriented Layered Halide Perovskite. *ACS Nano* **2022**, *16* (2), 2942–2952. https://doi.org/10.1021/acsnano.1c10098.

(14) Mao, L.; Wu, Y.; Stoumpos, C. C.; Traore, B.; Katan, C.; Even, J.; Wasielewski, M. R.; Kanatzidis, M. G. Tunable White-Light Emission in Single-Cation-Templated Three-Layered 2D Perovskites $(CH_3CH_2NH_3)_4Pb_3Br_{10-x}Cl_x$. *J. Am. Chem. Soc.* **2017**, *139* (34), 11956–11963. https://doi.org/10.1021/jacs.7b06143.

(15) Fu, Y.; Hautzinger, M. P.; Luo, Z.; Wang, F.; Pan, D.; Aristov, M. M.; Guzei, I. A.; Pan, A.; Zhu, X.; Jin, S. Incorporating Large A Cations into Lead Iodide Perovskite Cages: Relaxed Goldschmidt Tolerance Factor and Impact on Exciton–Phonon Interaction. *ACS Cent. Sci.* **2019**, *5* (8), 1377–1386. https://doi.org/10.1021/acscentsci.9b00367.

(16) Li, X.; Fu, Y.; Pedesseau, L.; Guo, P.; Cuthriell, S.; Hadar, I.; Even, J.; Katan, C.; Stoumpos, C. C.; Schaller, R. D.; Harel, E.; Kanatzidis, M. G. Negative Pressure Engineering with Large Cage Cations in 2D Halide Perovskites Causes Lattice Softening. *J. Am. Chem. Soc.* **2020**, *142* (26), 11486–11496. https://doi.org/10.1021/jacs.0c03860.

(17) Dolzhenko, Y. I.; Inabe, T.; Maruyama, Y. In Situ X-Ray Observation on the Intercalation of Weak Interaction Molecules into Perovskite-Type Layered Crystals $(C_9H_{19}NH_3)_2PbI_4$ and $(C_{10}H_{21}NH_3)_2CdCl_4$. *Bull. Chem. Soc. Jpn.* **1986**, *59* (2), 563–567. https://doi.org/10.1246/bcsj.59.563.

(18) Calabrese, J.; Jones, N. L.; Harlow, R. L.; Herron, N.; Thorn, D. L.; Wang, Y. Preparation and Characterization of Layered Lead Halide Compounds. *J. Am. Chem. Soc.* **1991**, *113* (6), 2328–2330. https://doi.org/10.1021/ja00006a076.

(19) Mitzi, D. B.; Feild, C. A.; Harrison, W. T. A.; Guloy, A. M. Conducting Tin Halides with a Layered Organic-Based Perovskite Structure. *Nature* **1994**, *369* (6480), 467–469. https://doi.org/10.1038/369467a0.

(20) Kagan, C. R.; Mitzi, D. B.; Dimitrakopoulos, C. D. Organic-Inorganic Hybrid Materials as Semiconducting Channels in Thin-Film Field-Effect Transistors. *Science* **1999**, *286* (5441), 945–947. https://doi.org/10.1126/science.286.5441.945.

(21) Mitzi, D. B.; Chondroudis, K.; Kagan, C. R. Design, Structure, and Optical Properties of Organic−Inorganic Perovskites Containing an Oligothiophene Chromophore. *Inorg. Chem.* **1999**, *38* (26), 6246–6256. https://doi.org/10.1021/ic991048k.

(22) Braun, M.; Tuffentsammer, W.; Wachtel, H.; Wolf, H. C. Pyrene as Emitting Chromophore in Organic–Inorganic Lead Halide-Based Layered Perovskites with Different Halides. *Chem. Phys. Lett.* **1999**, *307* (5), 373–378. https://doi.org/10.1016/S0009-2614(99)00526-6.

(23) Passarelli, J. V.; Fairfield, D. J.; Sather, N. A.; Hendricks, M. P.; Sai, H.; Stern, C. L.; Stupp, S. I. Enhanced Out-of-Plane Conductivity and Photovoltaic Performance in n = 1 Layered Perovskites through Organic Cation Design. *J. Am. Chem. Soc.* **2018**, *140* (23), 7313–7323. https://doi.org/10.1021/jacs.8b03659.

(24) Gao, Y.; Shi, E.; Deng, S.; Shiring, S. B.; Snaider, J. M.; Liang, C.; Yuan, B.; Song, R.; Janke, S. M.; Liebman-Peláez, A.; Yoo, P.; Zeller, M.; Boudouris, B. W.; Liao, P.; Zhu, C.; Blum, V.; Yu, Y.; Savoie, B. M.; Huang, L.; Dou, L. Molecular Engineering of Organic–Inorganic Hybrid Perovskites Quantum Wells. *Nat. Chem.* **2019**, *11* (12), 1151–1157. https://doi.org/10.1038/s41557-019-0354-2.

(25) Smith, I. C.; Smith, M. D.; Jaffe, A.; Lin, Y.; Karunadasa, H. I. Between the Sheets: Postsynthetic Transformations in Hybrid Perovskites. *Chem. Mater.* **2017**, *29* (5), 1868–1884. https://doi.org/10.1021/acs.chemmater.6b05395.

(26) Mitzi, D. B.; Medeiros, D. R.; Malenfant, P. R. L. Intercalated Organic−Inorganic Perovskites Stabilized by Fluoroaryl−Aryl Interactions. *Inorg. Chem.* **2002**, *41* (8), 2134–2145. https://doi.org/10.1021/ic011190x.

(27) Smith, M. D.; Pedesseau, L.; Kepenekian, M.; Smith, I. C.; Katan, C.; Even, J.; Karunadasa, H. I. Decreasing the Electronic Confinement in Layered Perovskites through Intercalation. *Chem. Sci.* **2017**, *8* (3), 1960–1968. https://doi.org/10.1039/C6SC02848A.

(28) Shin, M.; Kim, J.; Jung, Y.-K.; Ruoko, T.; Priimagi, A.; Walsh, A.; Shin, B. Low-Dimensional Formamidinium Lead Perovskite Architectures via Controllable Solvent Intercalation. *J. Mater. Chem. C* **2019**, *7* (13), 3945–3951. https://doi.org/10.1039/C9TC00379G.

(29) Sheikh, T.; Nawale, V.; Pathoor, N.; Phadnis, C.; Chowdhury, A.; Nag, A. Molecular Intercalation and Electronic Two Dimensionality in Layered Hybrid Perovskites. *Angew. Chem. Int. Ed.* **2020**, *59* (28), 11653–11659. https://doi.org/10.1002/anie.202003509.

(30) Passarelli, J. V.; Mauck, C. M.; Winslow, S. W.; Perkinson, C. F.; Bard, J. C.; Sai, H.; Williams, K. W.; Narayanan, A.; Fairfield, D. J.; Hendricks, M. P.; Tisdale, W. A.; Stupp, S. I. Tunable Exciton Binding Energy in 2D Hybrid Layered Perovskites through Donor–Acceptor Interactions within the Organic Layer. *Nat. Chem.* **2020**, *12* (8), 672–682. https://doi.org/10.1038/s41557-020-0488-2.

(31) Solis-Ibarra, D.; Karunadasa, H. I. Reversible and Irreversible Chemisorption in Nonporous-Crystalline Hybrids. *Angew. Chem. Int. Ed.* **2014**, *53* (4), 1039–1042. https://doi.org/10.1002/anie.201309786.

(32) Solis-Ibarra, D.; Smith, I. C.; Karunadasa, H. I. Post-Synthetic Halide Conversion and Selective Halogen Capture in Hybrid Perovskites. *Chem. Sci.* **2015**, *6* (7), 4054–4059. https://doi.org/10.1039/C5SC01135C.

(33) Aubrey, M. L.; Saldivar Valdes, A.; Filip, M. R.; Connor, B. A.; Lindquist, K. P.; Neaton, J. B.; Karunadasa, H. I. Directed Assembly of Layered Perovskite Heterostructures as Single Crystals. *Nature* **2021**, *597* (7876), 355–359. https://doi.org/10.1038/s41586-021-03810-x.

(34) Ramadan, A. J.; Noel, N. K.; Fearn, S.; Young, N.; Walker, M.; Rochford, L. A.; Snaith, H. J. Unravelling the Improved Electronic and Structural Properties of Methylammonium Lead Iodide Deposited from Acetonitrile. *Chem. Mater.* **2018**, *30* (21), 7737–7743. https://doi.org/10.1021/acs.chemmater.8b03084.

(35) Febriansyah, B.; Koh, T. M.; Rana, P. J. S.; Hooper, T. J. N.; Ang, Z. Z.; Li, Y.; Bruno, A.; Grätzel, M.; England, J.; Mhaisalkar, S. G.; Mathews, N. Hybrid 2D $[Pb(CH_3NH_2)I_2]_n$ Coordination Polymer Precursor for Scalable Perovskite Deposition. *ACS Energy Lett.* **2020**, *5* (7), 2305–2312. https://doi.org/10.1021/acsenergylett.0c00781.

(36) Soe, C. M. M.; Nagabhushana, G. P.; Shivaramaiah, R.; Tsai, H.; Nie, W.; Blancon, J.-C.; Melkonyan, F.; Cao, D. H.; Traoré, B.; Pedesseau, L.; Kepenekian, M.; Katan, C.; Even, J.; Marks, T. J.; Navrotsky, A.; Mohite, A. D.; Stoumpos, C. C.; Kanatzidis, M. G. Structural and Thermodynamic Limits of Layer Thickness in 2D Halide Perovskites. *Proc. Natl. Acad. Sci.* **2019**, *116* (1), 58–66. https://doi.org/10.1073/pnas.1811006115.

(37) Mao, L.; Morgan, E. E.; Li, A.; Kennard, R. M.; Hong, M. J.; Liu, Y.; Dahlman, C. J.; Labram, J. G.; Chabinyc, M. L.; Seshadri, R. Layered Hybrid Lead Iodide Perovskites with Short Interlayer Distances. *ACS Energy Lett.* **2022**, *7* (8), 2801–2806. https://doi.org/10.1021/acsenergylett.2c01321.

(38) Mączka, M.; Ptak, M.; Gągor, A.; Stefańska, D.; Sieradzki, A. Layered Lead Iodide of $[Methylhydrazinium]_2PbI_4$ with a Reduced Band Gap: Thermochromic Luminescence and Switchable Dielectric Properties Triggered by Structural Phase Transitions. *Chem. Mater.* **2019**, *31* (20), 8563–8575. https://doi.org/10.1021/acs.chemmater.9b03775.

(39) Jung, M.-H. Stacking of Layered Halide Perovskite from Incorporating a Diammonium Cation into Three-Dimensional Perovskites. *Langmuir* **2019**, *35* (50), 16444–16458. https://doi.org/10.1021/acs.langmuir.9b02524.

(40) Soe, C. M. M.; Stoumpos, C. C.; Kepenekian, M.; Traoré, B.; Tsai, H.; Nie, W.; Wang, B.; Katan, C.; Seshadri, R.; Mohite, A. D.; Even, J.; Marks, T. J.; Kanatzidis, M. G. New Type of 2D Perovskites with Alternating Cations in the Interlayer Space, $(C(NH2)_3)(CH_3NH_3)_nPb_nI_{3n+1}$: Structure, Properties, and Photovoltaic Performance. *J. Am. Chem. Soc.* **2017**, *139* (45), 16297–16309. https://doi.org/10.1021/jacs.7b09096.

(41) Nazarenko, O.; Kotyrba, M. R.; Wörle, M.; Cuervo-Reyes, E.; Yakunin, S.; Kovalenko, M. V. Luminescent and Photoconductive Layered Lead Halide Perovskite Compounds Comprising Mixtures of Cesium and Guanidinium Cations. *Inorg. Chem.* **2017**, *56* (19), 11552–11564. https://doi.org/10.1021/acs.inorgchem.7b01204.

(42) Dohner, E. R.; Hoke, E. T.; Karunadasa, H. I. Self-Assembly of Broadband White-Light Emitters. *J. Am. Chem. Soc.* **2014**, *136* (5), 1718–1721. https://doi.org/10.1021/ja411045r.

(43) Mao, L.; Wu, Y.; Stoumpos, C. C.; Wasielewski, M. R.; Kanatzidis, M. G. White-Light Emission and Structural Distortion in New Corrugated Two-Dimensional Lead Bromide Perovskites. *J. Am. Chem. Soc.* **2017**, *139* (14), 5210–5215. https://doi.org/10.1021/jacs.7b01312.

(44) Febriansyah, B.; Lekina, Y.; Kaur, J.; Hooper, T. J. N.; Harikesh, P. C.; Salim, T.; Lim, M. H.; Koh, T. M.; Chakraborty, S.; Shen, Z. X.; Mathews, N.; England, J. Formation of Corrugated n = 1 2D Tin Iodide Perovskites and Their Use as Lead-Free Solar Absorbers. *ACS Nano* **2021**, *15* (4), 6395–6409. https://doi.org/10.1021/acsnano.0c08204.

(45) Stoumpos, C. C.; Kanatzidis, M. G. The Renaissance of Halide Perovskites and Their Evolution as Emerging Semiconductors. *Acc. Chem. Res.* **2015**, *48* (10), 2791–2802. https://doi.org/10.1021/acs.accounts.5b00229.

(46) Cortecchia, D.; Neutzner, S.; Srimath Kandada, A. R.; Mosconi, E.; Meggiolaro, D.; De Angelis, F.; Soci, C.; Petrozza, A. Broadband Emission in Two-Dimensional Hybrid Perovskites: The Role of Structural Deformation. *J. Am. Chem. Soc.* **2017**, *139* (1), 39–42. https://doi.org/10.1021/jacs.6b10390.

(47) Febriansyah, B.; Borzda, T.; Cortecchia, D.; Neutzner, S.; Folpini, G.; Koh, T. M.; Li, Y.; Mathews, N.; Petrozza, A.; England, J. Metal Coordination Sphere Deformation Induced Highly Stokes-Shifted, Ultra Broadband Emission in 2D Hybrid Lead-Bromide Perovskites and Investigation of Its Origin. *Angew. Chem. Int. Ed.* **2020**, *59* (27), 10791–10796. https://doi.org/10.1002/anie.201915708.

(48) Han, X.-B.; Jing, C.-Q.; Zu, H.-Y.; Zhang, W. Structural Descriptors to Correlate Pb Ion Displacement and Broadband Emission in 2D Halide Perovskites. *J. Am. Chem. Soc.* **2022**, *144* (40), 18595–18606. https://doi.org/10.1021/jacs.2c08364.

(49) Stoumpos, C. C.; Malliakas, C. D.; Kanatzidis, M. G. Semiconducting Tin and Lead Iodide Perovskites with Organic Cations: Phase Transitions, High Mobilities, and Near-Infrared Photoluminescent Properties. *Inorg. Chem.* **2013**, *52* (15), 9019–9038. https://doi.org/10.1021/ic401215x.

(50) Kepenekian, M.; Traore, B.; Blancon, J.-C.; Pedesseau, L.; Tsai, H.; Nie, W.; Stoumpos, C. C.; Kanatzidis, M. G.; Even, J.; Mohite, A. D.; Tretiak, S.; Katan, C. Concept of Lattice Mismatch and Emergence of Surface States in Two-Dimensional Hybrid Perovskite Quantum Wells. *Nano Lett.* **2018**, *18* (9), 5603–5609. https://doi.org/10.1021/acs.nanolett.8b02078.

(51) Robinson, K.; Gibbs, G. V.; Ribbe, P. H. Quadratic Elongation: A Quantitative Measure of Distortion in Coordination Polyhedra. *Science* **1971**, *172* (3983), 567–570. https://doi.org/10.1126/science.172.3983.567.

(52) Momma, K.; Izumi, F. VESTA 3 for Three-Dimensional Visualization of Crystal, Volumetric and Morphology Data. *J. Appl. Crystallogr.* **2011**, *44* (6), 1272–1276. https://doi.org/10.1107/S0021889811038970.

(53) Sheikh, M. A. K.; Kowal, D.; Mahyuddin, M. H.; Cala', R.; Auffray, E.; Witkowski, M. E.; Makowski, M.; Drozdowski, W.; Wang, H.; Dujardin, C.; Cortecchia, D.; Birowosuto, M. D. $A_2B_{n-1}Pb_nI_{3n+1}$ (A = BA, PEA; B = MA; n = 1, 2): Engineering Quantum-Well Crystals for High Mass Density and Fast Scintillators. *J. Phys. Chem. C* **2023**, *127* (22), 10737–10747. https://doi.org/10.1021/acs.jpcc.3c00824.

(54) Quan, L. N.; Yuan, M.; Comin, R.; Voznyy, O.; Beauregard, E. M.; Hoogland, S.; Buin, A.; Kirmani, A. R.; Zhao, K.; Amassian, A.; Kim, D. H.; Sargent, E. H. Ligand-Stabilized Reduced-Dimensionality Perovskites. *J. Am. Chem. Soc.* **2016**, *138* (8), 2649–2655. https://doi.org/10.1021/jacs.5b11740.

(55) Zhang, J.; Langner, S.; Wu, J.; Kupfer, C.; Lüer, L.; Meng, W.; Zhao, B.; Liu, C.; Daum, M.; Osvet, A.; Li, N.; Halik, M.; Stubhan, T.; Zhao, Y.; Hauch, J. A.; Brabec, C. J. Intercalating-Organic-Cation-Induced Stability Bowing in Quasi-2D Metal-Halide Perovskites. *ACS Energy Lett.* **2022**, *7* (1), 70–77. https://doi.org/10.1021/acsenergylett.1c02081.

(56) Zhumekenov, A. A.; Saidaminov, M. I.; Mohammed, O. F.; Bakr, O. M. Stimuli-Responsive Switchable Halide Perovskites: Taking Advantage of Instability. *Joule* **2021**, *5* (8), 2027–2046. https://doi.org/10.1016/j.joule.2021.07.008.

(57) De Bastiani, M.; Saidaminov, M. I.; Dursun, I.; Sinatra, L.; Peng, W.; Buttner, U.; Mohammed, O. F.; Bakr, O. M. Thermochromic Perovskite Inks for Reversible Smart Window Applications. *Chem. Mater.* **2017**, *29* (8), 3367–3370. https://doi.org/10.1021/acs.chemmater.6b05112.

(58) Sheldrick, G. M. SHELXT – Integrated Space-Group and Crystal-Structure Determination. *Acta Crystallogr. Sect. A Found. Adv.* **2015**, *71* (1), 3–8. https://doi.org/10.1107/S2053273314026370.

(59) Sheldrick, G. M. Crystal Structure Refinement with SHELXL. *Acta Crystallogr. Sect. C Struct. Chem.* **2015**, *71* (1), 3–8. https://doi.org/10.1107/S2053229614024218.

(60) Kresse, G.; Furthmüller, J. Efficient Iterative Schemes for Ab Initio Total-Energy Calculations Using a Plane-Wave Basis Set. *Phys. Rev. B* **1996**, *54* (16), 11169–11186. https://doi.org/10.1103/PhysRevB.54.11169.

(61) Kresse, G.; Joubert, D. From Ultrasoft Pseudopotentials to the Projector Augmented-Wave Method. *Phys. Rev. B* **1999**, *59* (3), 1758–1775. https://doi.org/10.1103/PhysRevB.59.1758.

(62) Vega, D.; Almeida, D. AIM-UC: An Application for QTAIM Analysis. *J. Comput. Methods Sci. Eng.* **2014**, *14* (1–3), 131–136. https://doi.org/10.3233/JCM-140491.

(63) Arunan, E.; Desiraju, G. R.; Klein, R. A.; Sadlej, J.; Scheiner, S.; Alkorta, I.; Clary, D. C.; Crabtree, R. H.; Dannenberg, J. J.; Hobza, P.; Kjaergaard, H. G.; Legon, A. C.; Mennucci, B.; Nesbitt, D. J. Definition of the hydrogen bond (IUPAC Recommendations 2011). *Pure Appl. Chem.* **2011**, *83* (8), 1637–1641. https://doi.org/10.1351/PAC-REC-10-01-02.

(64) Emamian, S.; Lu, T.; Kruse, H.; Emamian, H. Exploring Nature and Predicting Strength of Hydrogen Bonds: A Correlation Analysis Between Atoms-in-Molecules Descriptors, Binding Energies, and Energy Components of Symmetry-Adapted Perturbation Theory. *J. Comput. Chem.* **2019**, *40* (32), 2868–2881. https://doi.org/10.1002/jcc.26068.